

# Exploring Young Stellar Variability with Gaia DR3 light curves

C. Mas<sup>1</sup>, J. Roquette<sup>1</sup>, M. Audard<sup>1</sup>, M. Madarász<sup>2,3</sup>, G. Marton<sup>2,3</sup>, D. Hernandez<sup>4</sup>, I. Gezer<sup>2,3</sup>, and O. Dionatos<sup>5</sup>

<sup>1</sup> Department of Astronomy, University of Geneva, Chemin Pegasi 51, 1290 Versoix, Switzerland

<sup>2</sup> Konkoly Observatory, Research Centre for Astronomy and Earth Sciences, Hungarian Research Network (HUN-REN), Konkoly Thege Miklós Út 15-17, 1121 Budapest, Hungary

<sup>3</sup> CSFK, MTA Centre of Excellence, Budapest, Konkoly Thege Miklós út 15-17., H-1121, Hungary

<sup>4</sup> Universität Wien, Institut für Astrophysik, Türkenschanzstrasse 17, 1180 Wien, Austria

<sup>5</sup> Natural History Museum Vienna, Burgring 7, 1010 Vienna, Austria

## ABSTRACT

**Context.** Photometric variability is a defining characteristic of young stellar objects (YSO), which can be traced back to a range of physical processes taking place at different stages of young stars' formation and early evolution. The Gaia third Data Release (GDR3) has provided an unprecedented dataset of photometric time series, including 79 375 light curves for sources classified as YSO candidates. Thanks to its all-sky coverage, Gaia provides a unique opportunity for large-scale studies of YSO variability.

**Aims.** Our goal was to characterise the GDR3 sample of YSO variables to better identify the recurrence of YSO variability modes (due to accretion, extinction, rotation modulation, etc.). We make a pilot study of the applicability of the asymmetry ( $M$ ) and periodicity ( $Q$ ) variability metrics to characterise YSO variability with Gaia light curves. By adapting the Q&M-metrics for sparse and long-term light curves, we seek to bridge the gap between low and high-cadence survey insights on YSO variability.

**Methods.** We adapted the Q&M methodology for Gaia. Through refined sample selection, we identified sources with appropriate sampling for the Q&M methodology. We used the Generalised Lomb Scargle periodogram and structure functions to derive characteristic timescales of variability.

**Results.** We successfully derived Q&M indices for 23 000 sources in the GDR3 YSO sample. These variables were then classified into eight variability morphological classes. We linked morphological classes with physical mechanisms by using  $H\alpha$  as a proxy of accretion and  $\alpha_{\text{IR}}$ -indices to gauge circumstellar material's presence.

**Conclusions.** We demonstrate that the Q&M metrics can be successfully applied to study Gaia's sparse time-series. We applied it successfully to distinguish between the various variability modes of YSOs. While our results are generally consistent with previous high-cadence, short-term studies, we find that GDR3's long timespan yields an enhanced variety of variability mechanisms.

**Key words.** Stars: variables: general – Stars: variables: T Tauri, Herbig Ae/Be – Accretion, accretion disks – Stars: formation – Stars: pre-main sequence Stars: rotation

## 1. Introduction

Gaia (Gaia Collaboration et al. 2016, 2023b) is a cornerstone mission by ESA, in operation since mid-2014. In 2022, the Gaia Data Release 3 (GDR3) provided photometric and astrometric observations for 1.8 billion stars. GDR3 included epoch photometry covering 34 months of the mission provided for 11 754 237 sources, among which were variable (stellar and extragalactic Eyer et al. 2023) and all sources in the field of view (FOV) of the Gaia Andromeda Photometric Survey (GAPS Evans et al. 2023).

The GDR3 variables were classified by the General Variability Detection (GVD) path into 25 classes using a supervised machine learning classifier (Rimoldini et al. 2023) with 79,375 of them classified as Young Stellar Objects (YSOs). This sample of YSO candidates was validated by Marton et al. (2023) by cross-matching with existing YSO catalogues from optical and infrared surveys, revealing that 40,000 sources were newly identified YSOs. In this paper, we further explore the GDR3 YSO variable sample by providing a more detailed look at their variability modes.

Variability is a prevalent characteristic of YSOs, observed throughout their entire electromagnetic spectrum (Joy 1945; Herbst et al. 1994; Stelzer et al. 2007; Carpenter et al. 2001; Morales-Calderón et al. 2011; Venuti et al. 2015; Roquette et al. 2020). This variability can be traced back to a wide range of

physical mechanisms that take place in the formation and evolution of young stars, including mass accretion, star-disk interaction, disk dissipation, and outflows, among others (e.g. Fischer et al. 2023). Understanding YSO variability is thus fundamental to advancing our knowledge of how stars form and evolve during their first million years.

Attempts to devise variability classification schemes capable of grasping the assortment of observed YSO light curves have been made since the 1990s (e.g. Herbst et al. 1994). Although light-curve characteristics such as amplitude, timescale, and periodicity were recurrent ingredients, these earlier classification schemes were limited to the specific data for which they were designed. Based on an initial sample of 162 YSOs in the young cluster NGC 2264, Cody et al. (2014) proposed a new morphology classification scheme for YSO light curves. This scheme stems from two variability metrics designed to quantify the level of asymmetry ( $M$ -index) and periodicity ( $Q$ -index) in the light curves and allow for sorting sources into seven variability classes: strictly periodic, eclipsing binary, quasi-periodic symmetric, quasi-periodic dippers, aperiodic dipper, burster, and stochastic; with two more classes, multi-periodic, and long-trend added to include sources with characteristics missed by the default Q&M classification. Previous research comparing Q&M classification results with proxies of young stellar evolu-

tion (e.g., disk IR excess and accretion-induced emission lines such as  $H\alpha$ ) helped to associate these classes with various physical mechanisms behind the variability of YSOs with an emerging scenario where strictly periodic light curves are attributed to magnetically induced cold spots on the stellar surface viewed from high-inclination angles (e.g. [Cody et al. 2022](#)). Higher-amplitude quasi-periodic symmetric light curves are associated with accretion-induced hot spots at the stellar surface (e.g. [Venuti et al. 2015](#); [Cody & Hillenbrand 2018](#)). Dipper variability is linked to the AA Tauri phenomenon (e.g. [Bouvier et al. 1999](#); [Alencar, S. H. P. et al. 2010](#)), where magnetic star-disk-interaction is thought to lift dusty disk material above the disk's midplane, leading to periodic or aperiodic occultation. Bursting variables have been correlated with observables indicating intense ongoing accretion, suggesting a common origin (e.g. [Stauffer et al. 2014](#)). Stochastic variability is thought to originate from accretion related processes combined with low viewing angles ([Cody & Hillenbrand 2018](#)). While the Q&M classification scheme was initially designed aiming applications to high-cadence space-based light curves from the *Convection, Rotation and planetary Transits satellite* (CoRoT [Auvergne et al. 2009](#)) and Spitzer telescope, it has since been employed in the context of varied epoch surveys including other high-cadence surveys such as Kepler mission K2 ([Cody & Hillenbrand 2018](#); [Venuti et al. 2021](#); [Cody et al. 2022](#)), but also ground-based sources such as ZTF (Zwicky Transient Facility; [Hillenbrand et al. 2022](#); [Wang et al. 2023](#); [Jiang & Hillenbrand 2024](#)), ASAS-SN ([Bredall et al. 2020](#)), and VVVX ([Ordenes-Huanca et al. 2024](#)).

In this paper, we present the results of a pilot study that addressed the applicability of the Q&M metrics to GDR3 light curves. Applying this methodology is challenging due to the sparse and unevenly spaced observational window resulting from Gaia's scanning law. Most sources have only 30 to 100 epoch observations spanning 900 days, which requires a complete adaptation of the original methodology introduced by [Cody et al. \(2014\)](#), based on a high-cadence 40-day-long light curve with more than 4,000 epochs. Still, Gaia offers all-sky coverage in contrast with the modest sample of a few hundred YSOs studied by high-cadence surveys, which also only focused on a handful of close-by star-forming regions. Hence, beyond the caveats of its sparse sampling, Gaia provides us the opportunity to derive general statistics of YSO variability from a more extensive and diverse sample. Additionally, the longer time coverage of Gaia allows us to probe longer timescales of variability, which are relevant for our understanding of the scope and prevalence of YSO variability mechanisms.

This paper is organised as follows. In Sect. 2 we describe the data used in this paper. Our first goal is to test the applicability of Q&M indices to GDR3 data. For that, in Sect. 3 we perform several tests to remove sources or epoch observations that might be affected by instrumental biases. We filtered the YSO sample by removing sources with too few data points, which might have spurious variability induced by the scan angle. Finally, we split the sample in two, depending on the variability level. The high-variability sample was used to benchmark our methodology. In Sect. 4, we describe our process to implement Q&M with GDR3, with timescales derived using generalised Lomb-Scargle periodograms or structure functions. We also discuss the cases where no reliable timescale is found or those where the timescale is too long compared to the full light-curve duration. Sect. 5 presents the results on the Q&M-index, timescales, and morphological classes. We put the Q&M-index in relation with disk properties and the evolutionary stage of our samples, using

the  $\alpha_{\text{IR}}$  index and  $H\alpha$  emission line. In Sect. 6, we discuss our results and present a few light curves from each class, discussing the typical timescale, amplitude, and physical mechanisms behind them. We further discuss the limitations of our methods and how our results compare to previous high-cadence and ZTF studies. Finally, we summarise our work in Sect. 7.

## 2. Data

### 2.1. Epoch data

GDR3 epoch data cover 34 months of Gaia operation from July 25, 2014 to May 28, 2017. We used two epoch photometry datasets from GDR3:

YSO sample: composed of 79,375 variable sources identified as YSO candidates as part of GDR3's variability processing ([Eyer et al. 2023](#); [Rimoldini et al. 2023](#); [Marton et al. 2023](#)). GAPS: The Gaia Andromeda Photometric Survey (GAPS [Evans et al. 2023](#)) released epoch photometry for over 1.2 million sources located in a region of  $5.5^\circ$  radius centred on Andromeda. GAPS included the release of epoch photometry for both variable and sources not identified as variables in DR3, showcasing the full power of Gaia's epoch data. The existence of stars with no variability detected by Gaia in GAPS allowed us to benchmark for our variability investigations.

Due to Gaia's scanning law, the number of transits per source highly depends on the sky position. This is illustrated in Fig. 1. For the YSO sample, the number of epochs ranged from 14 to 138, and from 5 to 110 for GAPS. On average, YSO light curves have more epoch observations than GAPS sources.

The YSO sample and the source properties (mean magnitude, RA, DEC, etc.) were retrieved from the [Gaia ESA Archive](#). Light curves were retrieved using the `astroquery.gaia` package ([Ginsburg et al. 2019](#)). For this study, we focused our analysis on  $G$ -band epoch data, as our primary interest lies in classifying variability types rather than YSO types. While using data from other bands ( $G_{BP}$ ,  $G_{RP}$ ) might help distinguish between specific YSO processes, it falls beyond the scope of this work.

### 2.2. Supplementary data

In Sect. 3.3, we use data from GDR3 spurious variability table (`vari_spurious_signals`) that was described in [Holl et al. \(2023\)](#) to flag sources affected by scan-angle spurious variability.

#### 2.2.1. Epoch data from previous literature

In Sect. 6, we compare our results with previous literature investigating YSO variability using K2 and ZTF light curves. In [Cody et al. \(2022\)](#), K2 light curves were employed to study sources in the Taurus star-forming region, with 61 sources in common with our YSO sample; their light curves were provided to us through private communication with the authors. [Hillenbrand et al. \(2022\)](#), [Wang et al. \(2023\)](#) and [Jiang & Hillenbrand \(2024\)](#) used ZTF light curves to study YSO variability in the North America and Pelican Nebulae Complex, the Perseus Molecular Cloud, and the Mon R2 region, respectively. These studies included 509 sources in our YSO sample. ZTF light curves for these sources were downloaded from the ZTF archive ([Masci et al. 2019](#)) through the ZTF data access tool at the NASA/IPAC Infrared Science Archive. The total timespan

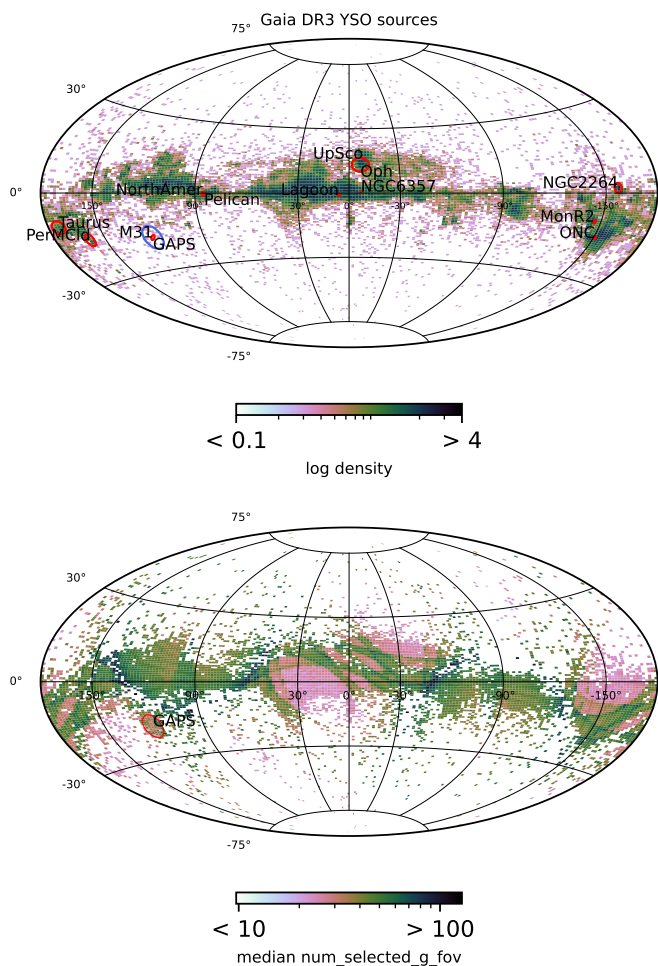


**Fig. 1.** Sky distribution of sources with GDR3 epoch data included in our study. Distributions are shown in galactic coordinates and Aitoff projection. *Top:* GDR3 YSO sample with colours indicating source density. The locations of prominent star-forming regions are highlighted in red circles and the location of the GAPS FOV in blue. *Bottom:* Both the YSO sample and GAPS sources are shown. The colour map shows the average number of data points in a light curve per bin.

of these light curves was limited to match the data released used in these previous studies, and the pre-processing of light curves followed the steps described in the previous studies.

## 2.2.2. YSO properties

To further validate our results in Sect. 6, we also matched our list of sources with catalogues with measurements related to the youth and evolutionary stages of YSOs. For measurements related to the  $H\alpha$  line, a proxy of accretion, we used:

NEMESIS (New Evolutionary Model for Early Stages of Stars with Intelligent Systems) Catalogue of YSOs for the Orion Star Formation Complex (Roquette et al. 2025) provides a curation of parameters related to the youth of sources in that region, providing  $H\alpha$  measurements for 5 231 sources in the YSO sample.

GALAH DR4 (The Galactic Archaeology with HERMES Survey Data Release 4; Buder et al. 2024) includes  $EW(H\alpha)$  measured from high-resolution spectroscopy for 2 085 sources in our catalogue.

LAMOST DR10 v2.0 (The General Survey of the Large Sky Area Multi-Object Spectroscopic Telescope Data; Zhao et al. 2012) includes  $EW(H\alpha)$  measured from low-resolution spectra for 2 172 sources.

Gaia-ESO Survey (Gilmore et al. 2022; Randich et al. 2022) DR5 5.1 Catalogue (Hourihane et al. 2023) provides  $EW(H\alpha)$  and full widths at 10% of the peak flux measurements derived from spectra observed with ESO’s UVES and GIRAFFE instruments, including data for 751 and 765 sources, respectively.

Gaia DR3 includes spectroscopic data products based on low-resolution spectra from the Blue and Red Photometers (De Angeli et al. 2023), which provides measurements of  $EW(H\alpha)$  with pseudo-equivalent widths estimated as part of the Extended Stellar Parametriser for Emission-Line Stars (ESP-ELS Creevey et al. 2023) for 56 964 sources in the YSO sample.

## 3. Data pre-processing

In this Section, we discuss the pre-processing and filtering steps to ensure only the most reliable light curves were kept in our sample. Fig. 2 summarises our filtering process workflow. Our first cleaning step was to remove epoch observations identified by GDR3 variability processing (Eyer et al. 2023) and flagged as `rejected_by_variability`.

### 3.1. Contamination by extragalactic sources

In GAPS, we excluded from our analysis 14,722 sources flagged with a probability over 0.8 of being a galaxy or a quasar, based on the Gaia DR3 classification probabilities <sup>1</sup> `classprob_dsc_combmod_galaxy` and `classprob_dsc_combmod_quasar` (Gaia Collaboration et al. 2023a). In contrast, only six sources were similarly removed from the YSO sample.

### 3.2. Minimum number of epochs

We performed tests (see App. A.1) to determine the minimum number of epochs in the light curve required to ensure statistically robust variability indices. All tests were carried out as a function of magnitude to account for the different levels of photometric noise in the sample. Based on these tests, we rejected light curves with fewer than 62 observations for G average magnitudes between 9.5 and 13.5 and 37 for those outside this range. This filtering step left 44 918 sources in our YSO sample (57% of the full catalogue). In GAPS, this step left 524 096 sources (42%).

### 3.3. Spurious variability

Holl et al. (2023) has identified spurious variability due to scan-angle effects (combination of Gaia’s mirror aspect ratio, spin-axis precession, and orbital period, Gaia Collaboration et al. 2016). Attempts to model and filter out the spurious frequencies caused by these scan-angle effects would require assumptions such as the underlying variability signal having a sinusoidal waveform, which are not reliable priors for YSO variability. Hence, instead of attempting to mask these signals, we have followed Gaia’s data processing literature (Holl et al. 2023;

<sup>1</sup> from GDR3 table `gaia_source`

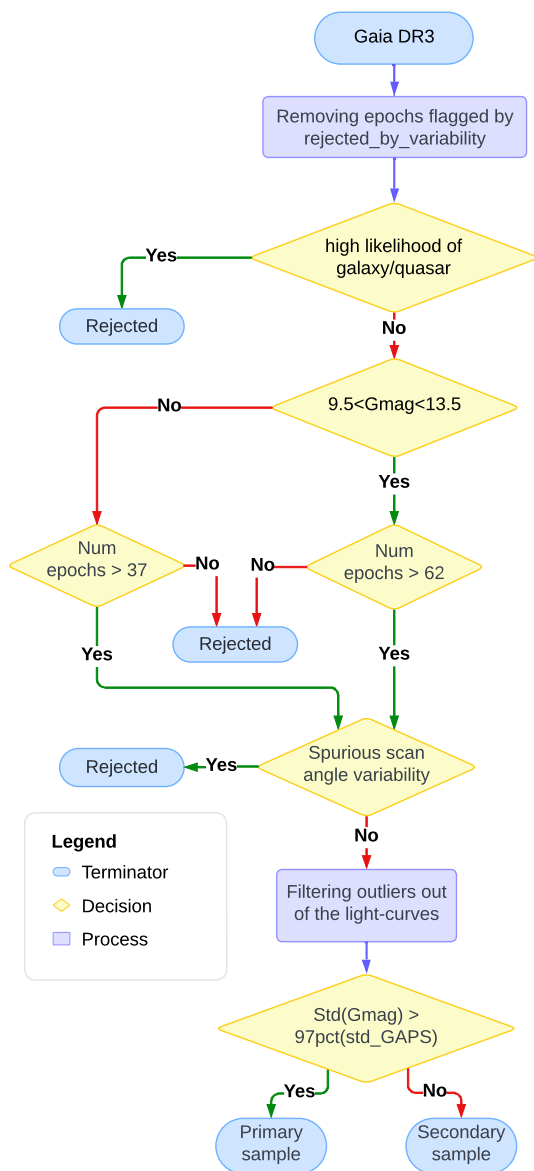


**Fig. 2.** Workflow illustrating the filtering steps before the Asymmetry and Periodicity analysis. It includes cleaning steps for accounting for extragalactic contamination (Sect. 3.1), removing sources with too few observed epoch (Sect. 3.2), removing sources likely affected by a spurious scan-angle (Sect. 3.3), removing epoch observations of spurious outliers (Sect. 3.4), and finally sorting the sources using variability level (Sect. 3.5).

Distefano et al. 2022) to identify and remove sources likely affected by spurious scan-angle signals (see App. A.2). Identifying and removing sources likely affected by spurious scan-angle signals allowed us to select 34,793 YSOs as reliable light curves (44% of the full catalogue). These sources constitute the full sample for this analysis, with some removals discussed in Sect. 4.2 due to residual overdensities caused by spurious scan angle effects identified after computing the timescales. In GAPS, our final sample contains 479 936 sources after this step (39%).

### 3.4. Outliers removal

Filtering large outliers is an important pre-processing step for studying the degree of asymmetry in the light curves as outliers can bias the M-index calculation (see Sect. 4.1). When dealing with high-cadence data, Cody et al. (2014) addressed this issue by  $5\sigma$ -clipping the light curves. In the case of CoRoT and K2, as the light curves were densely sampled, this approach was unlikely to remove relevant variability features. However, due to the sparsity of the GDR3 light curves, this type of filtering needs to be addressed more carefully to avoid removing relevant variability features from the light curve. We have done so in App. A.3, finding that 636 sources in our sample had at least one outlier removed. After this outlier removal, we also verified that all affected sources still fulfilled the minimum number of epochs required for light curve analysis.

### 3.5. Selection of highly variable sources

YSO candidates with GDR3 light-curves were all selected as variable by Gaia pipeline. However, our initial development tests showed that quasiperiodic symmetric variability largely dominates the lowest-amplitude light curves.

Since we wanted to test the applicability of the Q&M indices to a sample with a more significant relative incidence of variability modes, we split our sample in two: a primary sample with only the high-variability sources; and a secondary sample with all other sources passing the previous steps. The primary sample was used to develop the Q&M computation method.

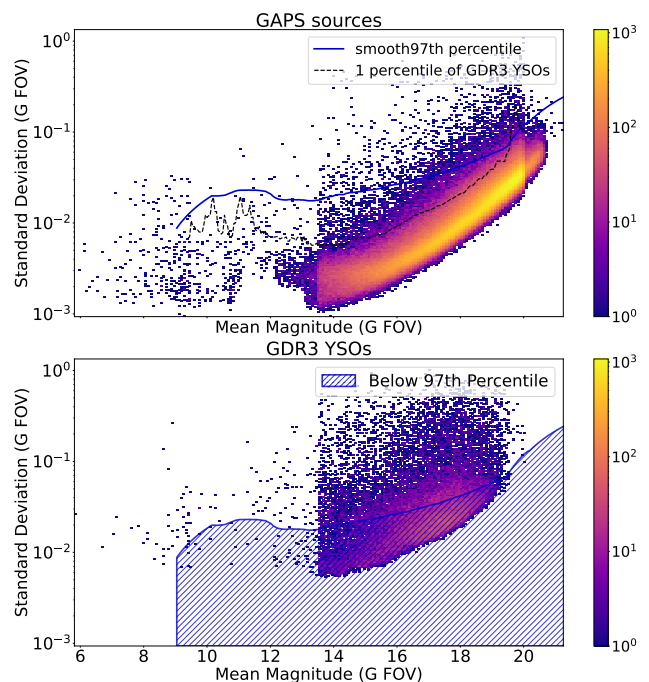


**Fig. 3.** Heatmap of the standard deviation distribution as a function of  $G$  magnitude. The colour bar indicates the number of sources. *Top:* Distribution for 479 936 GAPS sources. The solid blue line shows the smoothed 97<sup>th</sup> percentiles for the GAPS sample. The black dashed line shows the lower outline of GDR3 YSO distribution (1<sup>st</sup> percentile). *Bottom:* Distribution for the 34 793 sources in the pre-processed GDR3 YSO sample. The hashed area stresses out the sources below GAPS 97<sup>th</sup> rolling percentile in our secondary sample.

We defined a threshold for selecting the most significant variables as a function of magnitude based on the intrinsic variabil-

ity of sources in the GAPS sample, which does not necessarily includes only variable sources. A subsample of 479 334 GAPS sources passed all preprocessing steps described in this section. Fig. 3 shows the standard deviation (std) distribution as a function of magnitude for this sample, where std is our proxy of variability for this section. We derived a threshold based on the 97<sup>th</sup> percentile of the GAPS distribution, estimated by binning the GAPS std distribution using 0.05 mag bins from  $G = 9.1$  to 21.9 mag. Each magnitude bin is required to contain at least 500 sources, and bin sizes were sometimes increased by a factor of 1.1 until this minimum number of sources was satisfied. The 97<sup>th</sup> percentile was then calculated within each bin, and a Savitzky-Golay filter (Savitzky & Golay 1964) was applied to smooth it, resulting in the percentile curve shown in Fig. 3. This percentile curve was used to select 10,739 highly variable YSOs ( $\sim 13.5\%$  of the initial YSO sample) as part as the primary sample. A secondary sample of 24,054 YSOs below the 97<sup>th</sup> percentile is also discussed.

## 4. Methods

### 4.1. Asymmetry and Periodicity metrics

We explored the applicability of the periodicity (Q-index) and asymmetry (M-index) variability indices to characterise the GDR3 light curves. The Q-index is defined as (Cody et al. 2014; Hillenbrand et al. 2022):

$$Q = \frac{\text{std}_r^2 - \langle \sigma^2 \rangle}{\text{std}_m^2 - \langle \sigma^2 \rangle}, \quad (1)$$

where  $\text{std}_r^2$  is the variance of the residuals of the signal,  $\text{std}_m^2$  is the variance of the original light curve, and  $\langle \sigma^2 \rangle$  is the typical uncertainty (calculated here as the average of all squared errors associated with the data). The Q-index is thus a measure of the ratio of the variance of the residuals to the light curve's general variance. Lower Q values close to zero indicate high periodicity. In contrast, higher Q values (close to unity) reflect irregular or stochastic variability, with no apparent dominant periodic behaviour. The calculation of the Q-index assumes that the light curve contains a signal that may repeat at a characteristic timescale. This signal can be modelled by phase-folding the light curve to this characteristic timescale and employing a smoothing technique to model the signal's average waveform. A residual curve is then calculated as the difference between the raw-light curve and this waveform.

The M-index is defined as:

$$M = \frac{\langle m_{10\%} \rangle - m_{50\%}}{\sigma_m}, \quad (2)$$

where  $\langle m_{10\%} \rangle$  is the mean of the top and bottom deciles of the light curve,  $m_{50\%}$  is the median of all data points, and  $\sigma_m$  is the standard deviation. The M index measures the asymmetry of the light curve by comparing the deviations of the top and bottom deciles relative to the median brightness. Using data points in magnitude, light curves with dipping behaviour have M greater than 0.25, those with bursts have M smaller than  $-0.25$  (it would be the opposite if the data were in flux), and symmetric light curves will have M-index values around 0.

### 4.2. Characteristic timescale

The capital step to quantify the periodicity with the Q-index is to derive a characteristic timescale of variability. Fig. 4 summarises

the steps and decision making for timescale derivation, detailed further in this section.

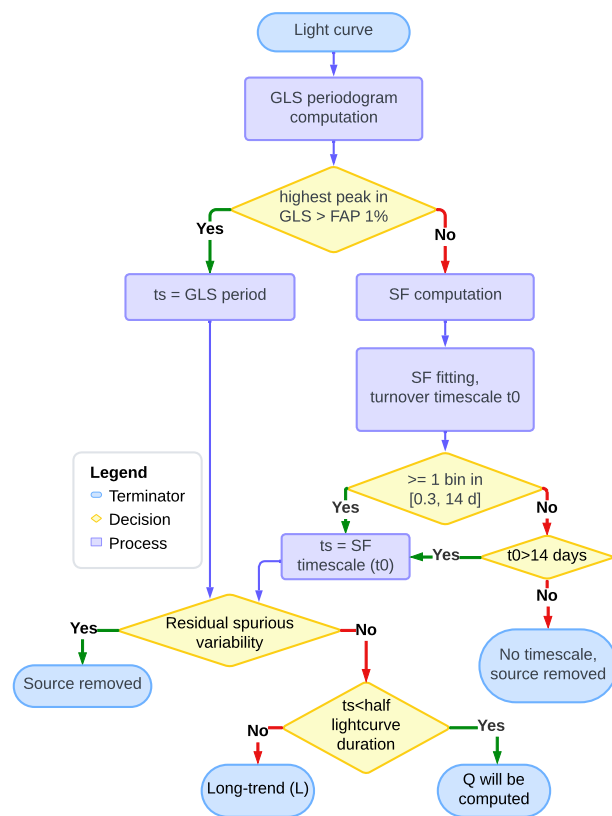


**Fig. 4.** Workflow illustrating the steps for deriving light curves' characteristic timescale, a required step for the Periodicity analysis with the Q-index. We first applied the Generalised Lomb-Scargle (GLS) periodogram to identify periodic timescales, assessing their reliability using the False Alarm Probability (FAP) (Sect. 4.2.1). If no reliable periodic timescale was found, we then computed the Structure Function (SF) to derive an aperiodic timescale (Sect 4.2.2). In cases where neither method provided a trustworthy timescale due to insufficient data, the source was removed from the analysis. A final step removes sources with timescales affected by spurious variability from the Gaia scan angle (Sect 4.3.).

#### 4.2.1. Generalised Lomb-Scargle periodogram

As a first step, we used Generalised Lomb-Scargle periodograms (Lomb 1976; Scargle 1982; Zechmeister & Kürster 2009)<sup>2</sup> to search for periodic variability in our sample and measure their period. We searched for periods between twice the median time step of the light curve (0.5 days) and the entire light curve duration (900 days). The frequency of the highest peak in the periodogram is selected as the most representative timescale of the light curve variability.

To evaluate the reliability of the timescales obtained with the GLS, we considered a false alarm probability level (FAL) of 1%, computed based on the method by Baluev (2008). Sources without a peak above the FAL were considered aperiodic. Fig. 5 shows examples of GLS periodograms for a periodic and an aperiodic source. A total of 24 067 sources ( $\sim 69\%$  of the YSO sam-

<sup>2</sup> We employed the Python implementation provided by Astropy (Astropy Collaboration et al. 2018; VanderPlas 2018)

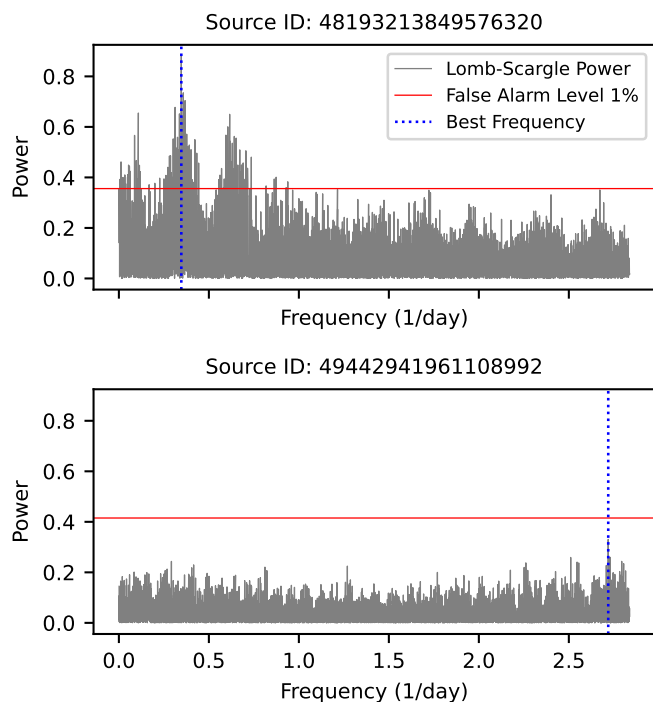


**Fig. 5.** Example of the two cases of GLS periodogram for timescale derivation. *Top:* The periodogram has a peak higher than the 1% FAP level; its frequency is used as the period. *Bottom:* The highest peak is lower than the 1% FAP level, and a non-periodic timescale is derived from the structure function.

ple) had their periodicity timescale successfully measured with the GLS. 3 721 of these timescales were longer than half of the total time span of the light curve. These were stored as evidence of long-timescale variability (long-trend) but were not used in the Q-index evaluation.

#### 4.2.2. Structure Function

In the previous section, 10 726 sources did not show any peak above the FAL in their GLS indicative of periodicity. Although these sources are likely aperiodic variables, their study with the Q-index still required the inference of a characteristic timescale for their aperiodic variability. In their original implementation, Cody et al. (2014) employed the PeakFind (Findeisen et al. 2015) algorithm for aperiodic timescale inference, which requires high cadence sampling to resolve detailed inflexions in light curves (Cody et al. 2022) and thus unattainable with sparsely sampled data sets such as GDR3.

Alternatively, we infer the timescale of aperiodic variability using structure functions (SF). SFs are widely used in Active Galactic Nucleus (AGN) variability studies (Simonetti et al. 1985; Kozłowski 2016) but have also been applied to variable stars (Eyer & Genton 1999) and YSOs (albeit in the context of high-cadence surveys; Venuti et al. 2021; Lakeland & Naylor 2022) to constrain variability timescales. In the context of Gaia DR2, structure functions were successfully used to investigate short timescale variables (Roelens et al. 2017).

Following Hughes et al. (1992) and Roelens et al. (2017), the SF is defined as:

$$\text{SF}(\tau) = \frac{1}{N(\tau)} \sum_{i>j} (m_i - m_j)^2, \quad (3)$$

where  $N(\tau)$  is the number of pairs separated by a time difference  $\tau$ , and  $m_i - m_j$  the magnitude difference for each pair  $N(\tau)$ .

Each bin corresponds to a range of time differences  $(\tau_1, \tau_2)$ , and is represented by its midpoint  $\tau$ . We selected all pairs of observations whose time separation  $\Delta t = t_i - t_j$  lies within this range to compute  $\text{SF}(\tau)$  at each bin.

We discretised the SF in Eq. (3) using logarithmically spaced time difference bins. To further adapt this binning strategy to unevenly sampled light curves, we introduced a tolerance factor  $\epsilon$ , which ensures that each bin contains enough pairs for a reliable calculation (Roelens et al. 2017). Bins that do not contain any pairs are excluded from the analysis. If a populated bin initially has too few pairs, its size is increased symmetrically until the minimum requirement of at least three pairs is met. With GDR3 data, we could compute SFs for time differences in the range 0.07–980 d (see Fig. B.1). The number of bins used was based on the number of epochs available for each light curve, with 1.5 times the number of epochs used for the number of bins.

For aperiodic variability, the SF typically shows three main regimes. A *noise-dominated regime*, where the SF remains roughly constant around the intrinsic noise level in the data. A *variability regime*, where the SF value increases until it peaks at the turnover timescale  $t_0$ . And a *plateau*, where beyond  $t_0$ , the SF flattens as no new variability occurs. To represent these three regimes, we fitted the SFs with a function of the form:

$$y = C_0 + C_1(1 - \exp(-\tau/t_0)), \quad (4)$$

where  $C_0$ ,  $C_1$ , and  $t_0$  are the fitting parameters and  $\tau$  is the time difference. In this model,  $C_0$  is related to intrinsic variability due to the uncertainty of the measurements and  $C_1$  is associated with the real signal variability amplitude. The final fitting parameter  $t_0$  is the turnover timescale, which marks the transition between the variability-dominated regime and the plateau and can be interpreted as the variability timescale in which we are interested.

We fit Eq. (4) to the SF using the MIGRAD routine (James & Roos 1975) implemented in Python as part of the `iminuit` library (Dembinski & et al. 2020). Initial guesses and limit values for the model parameters were based on inspection of the distribution of all SF shown in Fig. B.1 and were chosen as follows:  $C_0 = 0.02$ ,  $C_1 = 0.08$ ,  $t_0 = 15$  d for the initial guess. While  $C_0$  is in the range  $(10^{-5}, 0.07)$  mag<sup>2</sup>,  $C_1$  in  $(10^{-3}, 5.5)$  mag<sup>2</sup> and  $t_0$  in  $(0.07, 980)$  d. Examples of SF model fit results can be seen in Fig. 6.

The imposition of model parameter limits resulted in a relative excess of fit results with edge values. Hence, we filtered these results to remove spurious models within 5% from the edge values for  $C_0$ ,  $C_1$ , and for the lower limit of  $t_0$ . A total of 5 354 SF model fits were discarded at this step. Visual inspection of discarded SF models showed that these were typically sources with complex multimode variability, including different timescales and that cannot be successfully modelled by Equation (4), or sources with poorly sampled SF with a long time range without data (blind time range, further discussed below). An excess of upper limit values of  $t_0$  also existed, and we verified that these were typically related to light curves exhibiting a long-term trend (e.g., due to a gradual change in brightness) with a timescale longer than the timespan of GDR3 observations, where the SF continues to increase without ever reaching the plateau, in which case, we stored the timescale as evidence for long-term variability, but did not use them for Q-index evaluation.

In addition to the issue of edge values, 12 best-fit models were also discarded because they had limited  $\tau$  sampling around the derived timescale. This issue is further discussed in

the App. B, and it is introduced by GDR3 sparse time-series sampling, which for some sources results in a blind time range in the SF. For affected sources (see Fig. 6-bottom), no data points exist in the range  $\tau \sim 0.3 - 28$  days. Beyond this range, the SF show a flat distribution - hence, it is impossible for models to correctly identify the transition from the *variability regime* into the *plateau*.

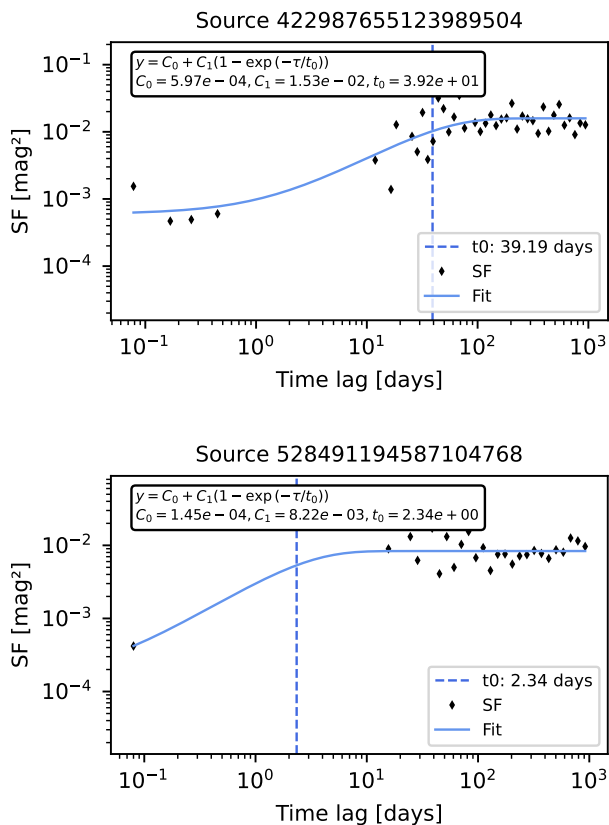


**Fig. 6.** Example structure functions for GDR3 sources in our sample. Both sources do not have a significant peak in the GLS periodogram, and thus we attempted to derive their dominant timescale with the SF method. The best fit derived from Minuit minimisation is plotted in blue. *Top:* Variability timescale of 39 days is inferred from the SF-fit. *Bottom:* Example of a source which suffered from a blind time range in its SF due to Gaia’s sparse sampling, thus a reliable timescale could not be derived.

The fits of the SF model in this section allowed us to estimate the aperiodic variability timescale for 4 118 sources. For 1 245 sources, the SF resulted in timescales in upper-edge values for  $t_0$ , or in timescales that were longer than half of the total time span of the light curve, and these were stored as evidence of long-trend but were not used in the Q-index evaluation. For 5 363, we were unable to derive a time scale of variability using the GLS or SF methods.

#### 4.3. Residual spurious variability

Following the discussion in App. A.4, we further remove 1 251 sources from our sample as their measured timescale coincided with typical timescales introduced by the spurious variability introduced by Gaia’s scan-angle effects (Sect. 3.3). After this final cleaning step, our final sample YSO light curves further analysed were composed of 28 179 sources, with 9 824 of these in

the primary sample, and 18 355 in the secondary sample. We only analysed sources for which we could derive a timescale.

#### 4.4. Q and M implementation and morphology classes

For the Q-index, once a characteristic timescale is derived, the light curve is folded to its corresponding phase. Next, we derive its waveform using a Savitzky-Golay filter with a window size of 25% of the phase and a second-order polynomial. This set of parameters allowed us to obtain waveforms representative of the ongoing variability while avoiding overfitting. The estimated waveform is then extracted from the data to obtain the residual curve. Finally, Q-indices can then be estimated with Eq. (1).

Following the seminal study by Cody et al. (2014), the Q and M indices can be used to gauge light-curve morphologies and sort variables into seven standard classes:

- Eclipsing binary (EB):  $Q < 0.11$  and  $M > 0.25$ ;
- Strictly Periodic (P):  $Q < 0.11$  and  $M < 0.25$ ;
- Quasi-periodic symmetric (QPS):  $0.11 \leq Q \leq 0.61$  and  $|M| \leq 0.25$ ;
- Quasi-periodic dippers (QPD):  $0.11 \leq Q \leq 0.61$  and  $M > 0.25$ ;
- Aperiodic dippers (APD):  $Q > 0.61$  and  $M > 0.25$ ;
- Bursters (B):  $Q > 0.11$  and  $M < -0.25$ ;
- Stochastic (S):  $Q > 0.61$  and  $|M| \leq 0.25$ ;

Previous literature included additional classes such as multiperiodic (MP), non-variable (NV) and long-trend (L). These classes are not based directly on the Q and M indices, but are defined based on the failure to apply Q&M methodology. The identification of multiperiodic variability in previous studies relied on the high cadence of their observations and required additional steps, including visual inspection of the light curves. We did not reproduce those steps as part of this study. The NV class was also excluded, since our sample is focused on light curves with enhanced variability. Long-trend variables were identified here as sources with inferred timescale longer than half of GDR3 timespan.

## 5. Results

### 5.1. Asymmetry and Periodicity indexes

Following the filtering steps in Sect. 3 and the methods in Sect. 4 we successfully derived Q-indices for 23 213 sources (8 385 in the primary sample) and M-indices for 28 179 sources (9 824; primary). Examples of light curves at different Q&M values are shown in Fig. 7 and Fig. 8, illustrating how we successfully adapted the Q&M methodology for use with Gaia DR3 light curves. In Fig. 7, light curves at low Q values are very well represented by the estimated periodic waveform. At intermediate Q-values, periodic waveforms are still found, but with an increased phase dispersion. At Q values close to unity, light curves are dominated by stochastic variability, where the timescales inferred can no longer be interpreted as a periodic timescale and the data points are stochastically distributed around the average. In Fig. 8, light curves with extreme asymmetries have M values farthest away from 0, with negative M values corresponding to variables with brightening events and positive M values corresponding to dimming events, while more symmetric light curves are closest to  $M = 0$ .

Fig. 9 shows the distribution of Q versus M for our sample. This general distribution peaks at  $Q \sim 0.43$  (quasi-periodic) and

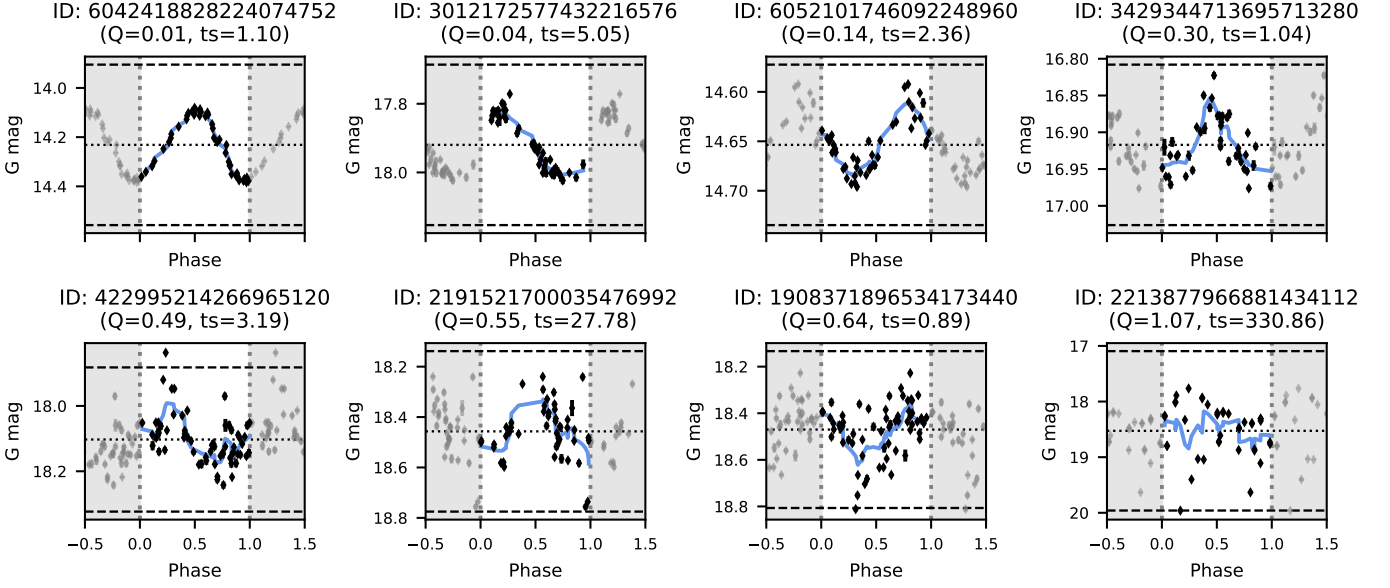


**Fig. 7.** Examples of phase-folded GDR3 light curves with increasing  $Q$  values from left to right. Black diamonds show phase-folded epoch photometry; the blue line is the estimated waveform (Savitzky-Golay filter). The grey area is the extended phase for better visualisation. Grey horizontal lines show the mean (dotted) and mean  $\pm 3\sigma$  (dashed)

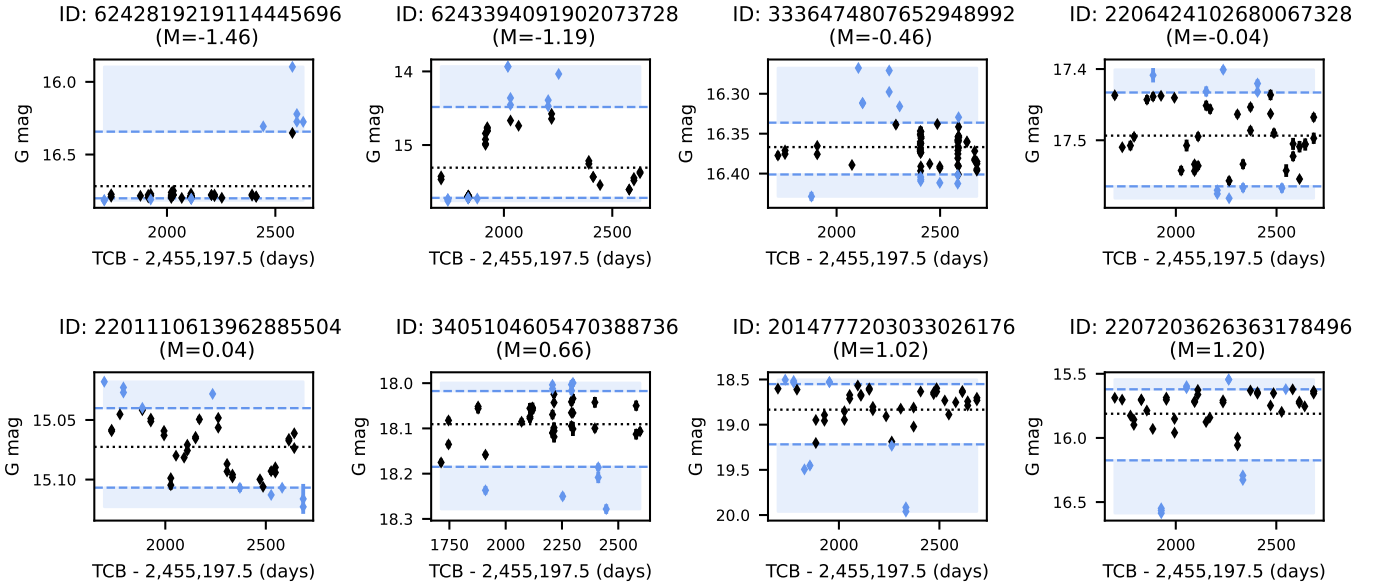


**Fig. 8.** Examples of GDR3 light curves with increasing  $M$  values from left to right. The blue diamonds are the data points of the top and bottom deciles of the curve; the grey dotted line shows the mean; the blue dashed lines the top and bottom deciles.

$M \sim 0.05$  (symmetric). The individual distributions of the  $Q$  and  $M$  indices are shown in Fig. 10, where we separate our sample by timescale method. As expected from the nature of the methodology involved in the derivation of variability timescales, the distribution of  $Q$  for sources with a periodic timescale derived by the GLS (in red) is mainly on the periodic/quasi-periodic region of the diagram, peaking at  $Q \sim 0.38$ , with the  $Q$ -index distribution for sources with aperiodic timescales derived from SFs peaking at  $Q \sim 0.64$ . For the  $M$ -index, sources with periodic timescales peak at  $\sim 0.02$ , and at  $\sim 0.15$  for aperiodic timescales, with the aperiodic distribution showing a tail towards dipping  $M$ -index values. Fig. 10 also compares the distribution of  $Q$  &  $M$ -indices for our primary and secondary samples, where

the differences for these two samples are also supported by Kolmogorov–Smirnov tests. Quasi-periodic variability is the most frequent mode among our sample, accounting for more than 69% of the sample. The secondary sample peaks at  $Q \sim 0.38$  and  $M \sim 0.02$ , being dominated by quasi-periodic symmetric sources - as mentioned in Sect. 3.5 the over-weight of this population of low-amplitude quasiperiodic symmetric sources on the general occurrence of variability classes was the motivation to discuss results as a function of a higher amplitude vs lower amplitude variable samples. The primary sample of variables peaks at  $Q \sim 0.44$  and  $M \sim 0.18$ , with a more relevant proportion of dipping and aperiodic variables in comparison to the secondary sample.

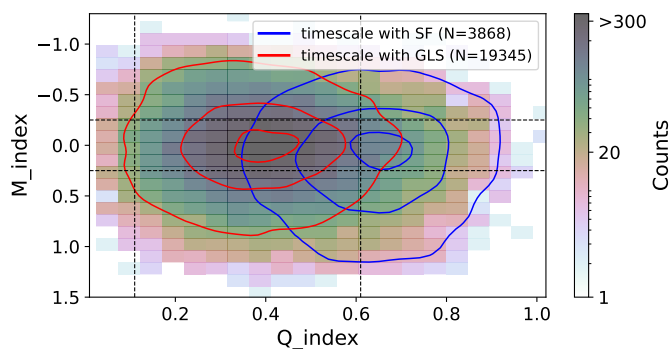


**Fig. 9.** Distribution of Q and M indices for 28 179 sources in the GDR3 YSO sample. Red lines contour the distribution of sources for which we computed the timescale with the GLS periodogram, and blue lines the ones with SF timescale (see Sect. 4.2). The dashed lines show the standard thresholds for the morphological class from Cody et al. (2014). In this Figure and all following Q&M distribution plots, the three contour curves contain 10, 50, and 90% of the data points, respectively.

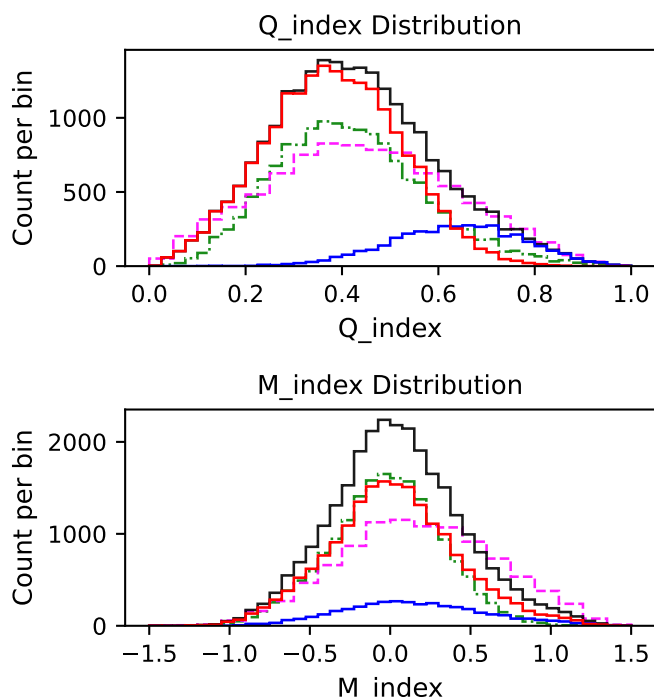


**Fig. 10.** Histograms for Q-index (top) and M-index (bottom) distributions. The Q-index distribution plot does not include the sources with a long timescale, contrary to the M-index one. In black, the full sample is shown. In red, the sources with a periodic timescale derived by the GLS. In blue, the sources with aperiodic timescale derived by the SF. The primary and secondary samples distributions are plotted respectively in dashed magenta lines and dashdotted green lines. Time on this plot and following is expressed in TCB (Temps-Coordonnée Barycentrique)

The classification scheme outlined in Sect. 4.4 was applied to classify light curves into seven morphological classes with an eighth class to account for long-trend variables. The count and frequency of sources in each class are summarised in Table 1. As already suggested by the Q&M distributions, dipper variability is the most common among the primary sample, with  $\sim 38\%$  of the primary sample showing aperiodic (APD) or quasi-periodic (QPD) dipper variability.

We also identified a total of 4 966 long-trend (L) variables, where the characteristic timescale derived was longer than half the total time span of the GDR3 observations (typically  $\sim 475$  days). These account for 3 721 periodic timescales derived with the GLS and 1 45 aperiodic timescales derived with the SF. We visually inspected a large fraction of these light curves and confirmed that a long-term trend was indeed present. These timescales are at the limit of GDR3 resolvable timescales and should be interpreted as a bottom limit for the real variability timescale, and hence we did not employ them for Q-index calculation, although we discuss them as part of our results.

## 5.2. Amplitude and timescales

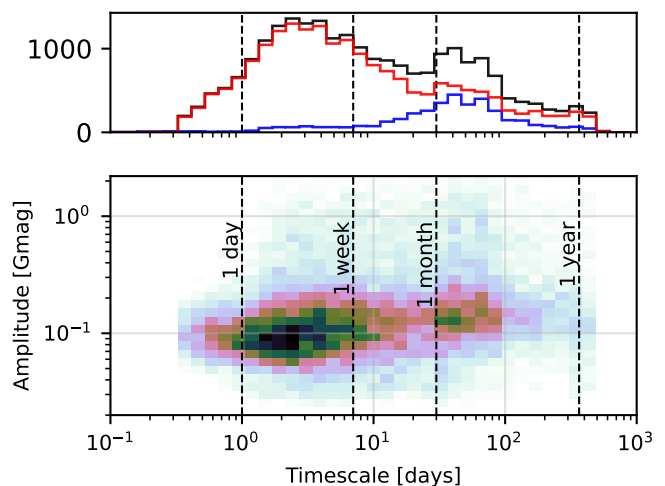


**Fig. 11.** *Top:* Timescale distribution for the full sample (black), 19 345 sources with GLS timescale (red) and 3 868 sources with an SF timescale (blue) *Bottom:* Distribution of amplitudes as a function of timescales for the full sample of 23 213 sources with derived timescale. This plot does not include sources with a long timescale.

We further complemented our results analysis with peak-to-peak (ptp) amplitudes and timescales measurements. We used the min-max amplitude as a measure of the ptp amplitude rather than the 5-95 percentile amplitude more commonly employed in the literature, as we found the latter to underestimate ptp amplitudes when applied to GDR3 sparse sampling. Throughout the discussion of results, we refer to timescales in the range 0.5 – 16 d as *rotation timescales*. Timescales larger than 20 d and less than about half of the duration ( $\sim 450$  days) of the observations are termed *intermediate timescales*. Timescales longer than half of the duration of the light curve are referred to as *long-trend timescales*.

Fig. 11 shows the distribution of amplitudes as a function of timescales for our sample, revealing a bimodal distribution of timescales with a population of sources with rotation-timescales (62%) and a second population of variables with intermediate timescales ( $\sim 24\%$  of the sample).

As detailed in Sect. 4.2.2 and App. B, a combination of factors such as the sparse sampling of GDR3 and the SF discretisation process makes the SF method inefficient for detecting aperiodic timescales in the range  $\sim 0.3 - 28$  d. Hence, if the GLS method was inefficient at detecting long timescales, this bimodality could be explained by the detection limits introduced by the combined use of these two methods. Conversely, Fig. 11 shows that the distribution of timescales measured with the GLS

**Table 1.** Counts and frequencies of sources per variability morphologic classes.

Class	Full sample					Primary					Secondary				
	count	Disk	CTTS	ts-ratio	ptp	count	Disk	CTTS	ts-ratio	ptp	count	Disk	CTTS	ts-ratio	ptp
P	286	17.1	13.7	13.4	0.19	199	17.6	14.6	26.6	0.22	87	11.5	8.7	5.8	0.10
QPS	9 514	20.2	14.8	2.6	0.15	2 362	42.1	36.6	1.4	0.31	7 15	13.0	6.1	3.3	0.09
QPD	5 439	39.4	24.7	1.8	0.35	2 886	62.1	40.6	1.3	0.57	2 553	13.7	4.5	2.5	0.09
APD	1 103	56.9	39.7	0.4	0.53	822	68.4	48.2	0.4	0.67	281	23.5	3.0	0.7	0.13
B	5 252	21.7	22.0	2.0	0.16	1 505	45.2	45.6	1.3	0.31	3 747	12.2	7.0	2.4	0.10
S	1 490	28.2	23.6	0.8	0.19	601	43.3	49.0	0.4	0.30	889	18.0	7.4	1.1	0.12
EB	129	17.1	11.4	23.6	0.20	95	16.8	14.1	91.0	0.24	34	17.7	0.0	6.8	0.10
L	4 966	21.1	11.0	-	0.16	1 354	40.0	33.6	-	0.37	3 612	14.1	2.5	-	0.09

**Notes.** Morphologic classes are defined as in Sect. 4.4, where EB: Eclipsing Binaries, P: Strictly Periodic, QPS: Quasi-periodic symmetric; QPD: Quasi-periodic dippers; APD: Aperiodic Dippers; B: Bursters; S: Stochastic; L: Long-timescale variables. Primary and secondary samples are detailed in Sect. 3.5. ‘Disk frequency’ indicates the frequency of stars with an envelope or presence of a thick disk as indicated by the  $\alpha_{\text{IR}}$  criteria discussed in Sect. 5.3.2. ‘CTTS frequency’ indicates the frequency of sources identified as CTTS in Sect. 5.3.1 in comparison with the total number of sources with  $H\alpha$  information. ‘ts-ratio’ indicates the ratio between sources with rotation against intermediate timescales. ‘ptp’ indicates the average peak-to-peak amplitude per class. The primary sample and secondary sample are detailed in Sect. 3.5.

method is itself bi-modal, with 28% of GLS-derived values at intermediate-timescales. Additionally, albeit much reduced in numbers, the SF timescale distribution accounts for  $\sim 6\%$  of rotation timescales. Another possible explanation would be that the intermediate-timescale population is the result of the spurious variability discussed in Sect. 3.3. However, we have addressed and mitigated the occurrence of residual spurious variability in our sample in App. A.4 and Sect. 4.3, where we discarded sources with timescales in the ranges typically susceptible to spurious variability. Finally, when comparing our results with previous studies using ZTF light curves (Sect. 6.3.2), we found that those previous studies also find a hint to similar bi-modality in timescales, with  $\sim 74\%$  vs  $\sim 9\%$  incidence of rotation and intermediate timescales. We are therefore confident that the observed bi-modality is real.

The two populations also show distinctive behaviour in ptp amplitudes, with rotation timescales showing average amplitudes of 0.18 mag (standard deviation 0.26) and intermediate timescales at 0.29 mag (0.38), and these differences are also supported by a Kolmogorov–Smirnov (KS) test.

### 5.3. Asymmetry and Periodicity metrics in the context of YSO’s observed properties

In this section, we examine our results in the context of quantities related to the physical characteristics of YSOs.

#### 5.3.1. Accreting vs. non-accreting sources

We used the data described in Sect. 2.2.2 to classify sources as Classical T Tauri Stars (CTTS) based on their  $H\alpha$  emission and as actively accreting sources. For equivalent width measurements, we employed spectral type-dependent criteria by Barrado y Navascués & Martín (2003) converted into Gaia  $G_{\text{BP}}-G_{\text{RP}}$  colours using the Pecaut & Mamajek (2013) empirical sequence. For full widths at 10% of the peak flux measurements, we used the White & Basri (2003) criterion to distinguish between CTTS and weak-lined TTS (WTTS). For 64 sources, we used qualitative flags that report  $H\alpha$  in emission (from Pettersson et al. 2014). When multiple  $H\alpha$  measurements were available, we considered that one measurement indicating a CTTS classification was enough to grant the source a classification as such. Specifically for  $\text{EW}(H\alpha)$  measurements from

ESP-ELS Gaia DR3 we have restricted our analysis to 7,318 sources with the absolute value of reported  $\text{EW}(H\alpha)$  larger than at least 5 times reported uncertainties. This decision was motivated by the limitations due to  $G_{\text{BP}}/G_{\text{RP}}$  spectral low resolution and its representation as Hermite function bases ( $R \sim 30 - 100$ ; De Angeli et al. 2023), where the identification of sources with large values of  $\text{EW}(H\alpha)$  are reliable, but where low accreting and non-accreting sources with  $\text{EW}(H\alpha)$  values closer to the stellar continuum may be confused within uncertainties.

In total, we could assign CTTS/WTTS labels to 13,802 sources in the YSO sample with at least one  $H\alpha$  measurement, 7 738 in the variable sample, and 2 829 in our primary variable sample with both Q&M derived, with 1 107 CTTSs and 1 722 WTTSs. The Q vs. M distribution for these sources is shown in Fig. 12, where we further distinguish between disk-bearing and diskless WTTS based on their  $\alpha_{\text{IR}}$ -index (see Sect. 5.3.2). The sample of sources with  $H\alpha$  information has a lower incidence of aperiodic sources, with only  $\sim 11\%$  of these compared to  $\sim 20\%$  in the full variable sample.

The Q&M distribution for diskless WTTS peaks at  $Q \sim 0.29$  and  $M \sim 0.04$ , with the distribution in Q shifted toward the intersection between strictly and quasiperiodic sources and a narrower distribution of M values concentrated toward symmetric M indexes. The subsample of actively accreting sources (CTTS) is mainly quasiperiodic, with their distribution peaking at  $Q \sim 0.42$  and  $M \sim 0.13$ . Compared to the diskless WTTS distribution, the CTTS is shifted towards larger Q values, with a much wider distribution of M values including more significant fractions of dippers and bursters. For disk-bearing WTTSs,  $Q \sim 0.38$  and  $M \sim 0.24$ , with the distribution presenting intermediary properties between the former two groups. Disk-bearing WTTSs show a smaller relative fraction of strictly periodic sources compared to diskless WTTS as well as an excess of quasiperiodic dippers with larger M-values compared to CTTSs.

To further support results discussion, Table 1 includes the CTTS frequency. This is defined as the percentage of CTTS sources among sources with  $H\alpha$  measurements and is interpreted here as a measure of the fraction of actively accreting sources within a sample. However, we note that  $H\alpha$  measurements are only possible for optically visible sources, thus this proxy will inevitably miss deeply embedded sources. Furthermore, we also note that the accretion process and the resulting  $H\alpha$ -emission are also highly variable (e.g. Sousa et al. 2016). Hence, although

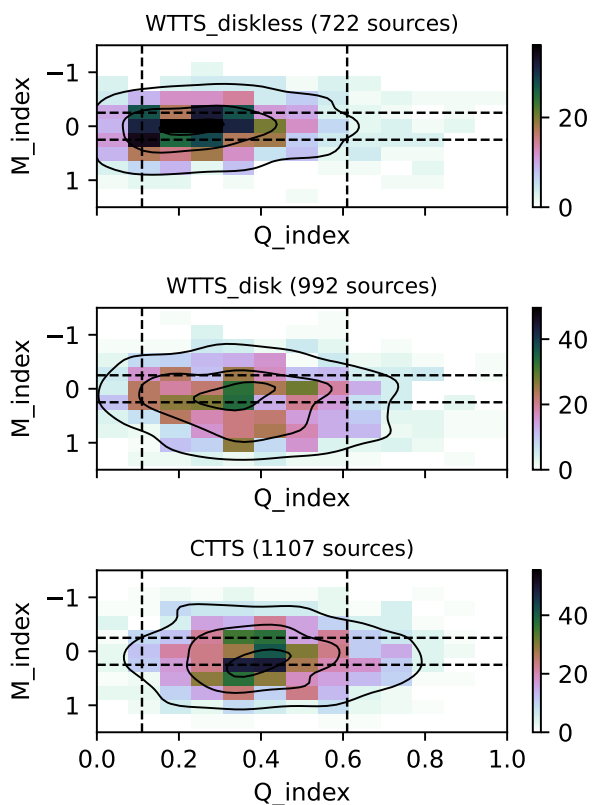


**Fig. 12.** Q vs. M distributions for sources in the primary sample with constrain of ongoing accretion based on observations of their  $H\alpha$  lines (see Sect. 5.3.1). The dashed lines separate the regions for the Q-M morphologies (see Sect. 4.4). *Top:* Sources with no observational indication of ongoing accretion (WTTS) and absence of a disk as identified from their IR SED. *Middle:* Sources with no observational indication of ongoing accretion (WTTS), but that had the presence of a disk as identified from their IR SED. *Bottom:* Sources identified as actively creating, CTTS.

strong  $H\alpha$  emission indicates ongoing accretion, the opposite is not always true, as the source may still be sporadically accreting over longer timescales although not in the specific season observed. CTTS fraction must thus be interpreted as a bottom limit of the true fraction of actively accreting sources.

### 5.3.2. Circumstellar disks

To gauge the influence of circumstellar disks on our variability results, we also examined the  $\alpha_{IR}$  indices for our sources. The  $\alpha_{IR}$  index is a measure of the slope of the IR spectral energy distribution (SED) and quantifies the contribution to the SED of infrared radiation re-emitted by material around YSOs. To estimate  $\alpha_{IR}$  we follow a similar procedure as the one in the NEMESIS YSO catalogue: We used the Vizier Photometry viewer tool to retrieve all previously published photometric data available at the Centre de données astronomiques de Strasbourg (Genova et al. 2000; Ochsenbein et al. 2000), and used data in the wavelength range  $2 - 24 \mu\text{m}$  to fit a linear model to measure  $\alpha_{IR}$ . Next, we employ an adaptation of the standard classification scheme for YSOs based on their  $\alpha_{IR}$  (Lada 1987; Andre et al. 1993; Greene et al. 1994), where, to facilitate our discussion, we name subclasses based on the dominant contributor to their SED: sources with significant contribution of their envelope have  $\alpha_{IR} > -0.3$  (483 sources in the primary sample), sources with a

thick disk have  $0.3 < \alpha_{IR} \leq -1.6$  (3 856 sources), sources with thin disks have  $-1.6 < \alpha_{IR} \leq -2.5$  (1 741 sources) and diskless sources have  $\alpha_{IR} < -2.5$ , (2 320 sources). Fig. 13 shows the Q vs. M distributions for each of these samples. Table 1 includes the frequency of sources with  $\alpha_{IR}$ -based evidence for the existence of an inner disk, which we define as the total number of sources classified as Envelope or Thick disk, divided by the total number of sources with derived  $\alpha_{IR}$ -index.

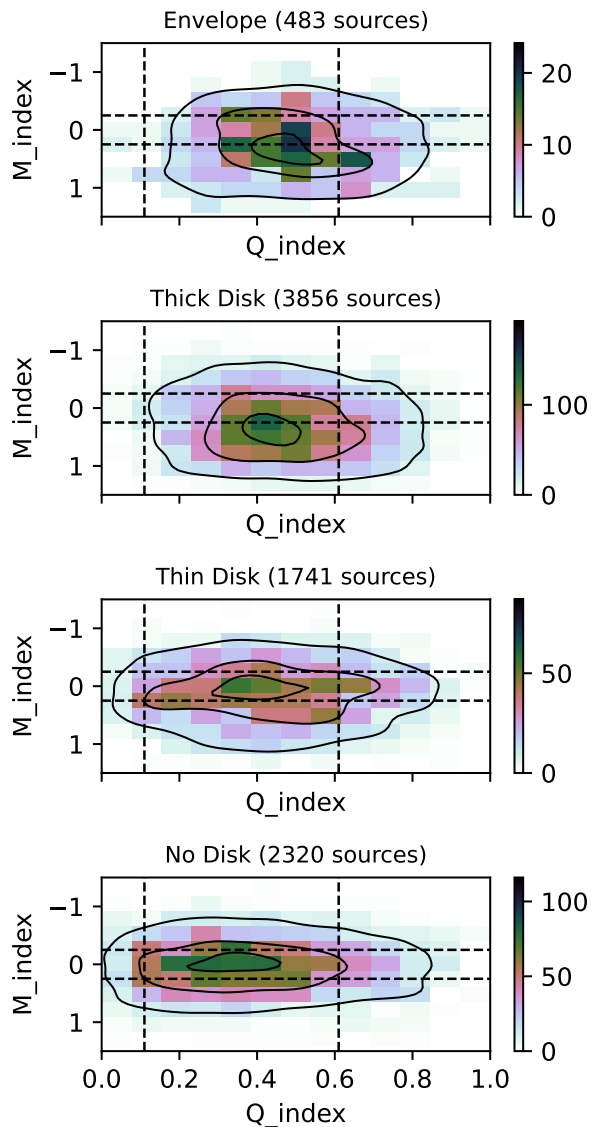


**Fig. 13.** Density distribution of sources in the Q-M diagram four sub-samples defined based on the  $\alpha_{IR}$  index (see Sect. 5.3.2). The dashed lines underline the Q-M morphologies (see Sect. 4.4). *Top:* sources with contribution of an envelope to their SED; *Middle-top:* sources with evidence for a thick-disk, *Middle-bottom:* sources with evidence for a thin disk, *Bottom:* diskless sources. The colour map shows the count density per bin.

KS tests between envelope and thick disk samples suggest that these samples share the same mother Q&M distribution. However, when examined in terms of the ratio between rotation and intermediate timescales, we find a 0.7 ratio for the envelope sample compared to a 1.0 ratio for the thick disk sample. Generally, Fig. 13 suggests a gradual transition towards a distribution

of M-indices that favours symmetry and a shift toward enhanced periodicity for more evolved YSO populations.

Several of the variability mechanisms in YSOs stem from the star-disk interaction process, where the young star magnetically interacts with its inner disk. Hence a relevant quantity included in Table 1 is the percentage of sources with  $\alpha_{\text{IR}}$  index indicative of the presence of a inner disk, which we define as  $\alpha_{\text{IR}} \geq -1.6$  and includes both sources with a thick disk or an envelope. We stress that these quantity also represent the bottom limit of the true frequencies. Our  $\alpha_{\text{IR}}$  are derived based on heterogeneous data available from previous publications and thus may be biased toward a lack of mid- and far-infrared data, which are only available all-sky within the context of *WISE* (Wright et al. 2010), with limited coverage for  $\lambda \gtrsim 5\mu\text{m}$ .

## 6. Discussion

The effectiveness of the Q&M-metrics for characterising YSO variability has been previously demonstrated in the literature with successful applications to high-cadence data from space telescopes and data with longer timespan but from ground-based telescopes. With the present study, we contributed to this body of research by demonstrating the applicability of the Q&M-metrics to Gaia's sparse, but high-precision, long-term data. With this applicability demonstrated, in this section we proceed to discuss the interpretation of our results given the morphological classes defined with Q&M.

### 6.1. Incidence of morphological classes across surveys

In this section, we discuss the incidence of morphological classes in different surveys. Here and in Sect. 6.2, literature comparison is discussed at the population level. A comparison of some individual sources in common between the surveys is presented in Sect. 6.3. Table 2 shows a comparison of the frequencies of variability morphology in different studies. Morphological classes from the literature are taken as reported, without review of their Q&M thresholds. Fig. 14 shows the distribution of amplitudes versus timescales for each morphological class. This includes our primary and secondary samples, as well as the main samples from the literature combined by type of survey, including high-cadence surveys (CoRoT and K2 Cody et al. 2014; Cody & Hillenbrand 2018; Venuti et al. 2021; Cody et al. 2022) and ground-based results (from ZTF; Hillenbrand et al. 2022; Wang et al. 2023; Jiang & Hillenbrand 2024). Detailed discussion of the properties of each morphological class are later presented in Sect. 6.2.

Discussion of results must thus be carried out while acknowledging survey-to-survey differences. First, in terms of sample size: our Gaia study included 9 824 YSOs in the primary sample and 18,355 in the secondary sample, while ZTF and high-cadence surveys included 1 031 and 549 sources, respectively. With much smaller sample sizes, previous studies heavily relied on visual inspection of light curves for classification, with Q&M thresholds adjusted by eye to maximise its correspondence with visually attributed morphological classes. Although infeasible in large-scale surveys such as Gaia, this empirical approach adopted in previous studies suggests that survey-to-survey adjustments of Q&M thresholds can help account for surveys' sampling limitations and may improve purity within morphological classes. In Sect. 4.4, we adopted Cody et al. (2014) original Q&M thresholds for morphological classification. As further discussed in Sect. 6.2, our results suggest that these thresholds

**Table 2.** Frequency of morphological classes for GDR3 light curves compared to results in previous studies.

Class	This Work	Previous Studies	
	Full Sample	High-cadence	ZTF
P	1.0	6.7	14.5
QPS	33.7	28.3	35.6
QPD	19.3	16.1	13.8
APD	3.9	15.7	10.0
B	18.6	17.6	8.9
S	5.3	12.8	14.0
EB	0.5	0.2	-
L	17.6	2.6	3.2

**Notes.** Frequency of variability classes (P, QPS, QPD, APD, B, S, EB, and L) are shown as a percentage of occurrence within the total sample. For previous studies, reported frequencies represent only the primary variability classifications, as multi-mode variability analysis was not systematically incorporated. In particular, for ZTF, the reported L fraction (3.2%) does not account for secondary classifications. If we did, the L fraction would be around 10.7%.

led to some contamination of symmetric light curves into asymmetric classes within our sample. With the ground truth of visual inspection further hindered by Gaia's sparse light-curves, an alternative approach would be to review Q&M thresholds based on simulated light curves. Although beyond the scope of the present study, our team has been exploring this approach as part of our preparations for Gaia DR4.

There are also source selection differences, where high-cadence surveys examined only disk-bearing sources, while both our results and ZTF's include all types of YSOs. Moreover, previous studies focused on individual star-forming regions, with much narrower age-distributions in comparison with the GDR3 all-sky sample. Notably, Cody et al. (2022) attempted to interpret the frequency distribution of morphological classes in different star-forming regions in light of their age. In our case, this type of interpretation is hindered by the lack of previous constraints in the age distribution of the GDR3 YSO catalogue. However, our investigations of  $\alpha_{\text{IR}}$ -indices in Sect. 5.3.2 revealed that 42% and  $\sim 32\%$  of our sample of variables had no indication of the presence of a disk or only a thin-disk contribution to their SEDs.

Given the enhanced fraction of diskless YSOs in our sample, cool spot variability, typically associated with P and QPS sources, is expected to be the most common in our sample. Although QPS is in fact the most common variability class, Table 2 shows that the frequency of P-variables is much lower than in previous studies. As further discussed in Sect. 6.2.1, beyond cadence and underlying noise, this can be attributed to cool-spot variability being unstable at timescales of the order of GDR3 observations. We note that cool-spot variability is a central feature of "solar-like variables", which are themselves a subgroup of Gaia DR3 variability classes (Distefano et al. 2022), where the authors report that between 53 to 72% of their 474 026 variables show unstable spot-variability (amplitude variation) during the observed time covered by GDR3. This helps explain not only our under-detection of the P-variable compared to previous studies, but also contributes to our enhanced detection of QPS variables. Table 2 also indicates that ZTF studies, which likewise include diskless sources, show a much larger sample of P and QPS sources in comparison to high-cadence surveys. However, ZTF studies use much larger Q thresholds to account for the higher noise from ground-based observations.

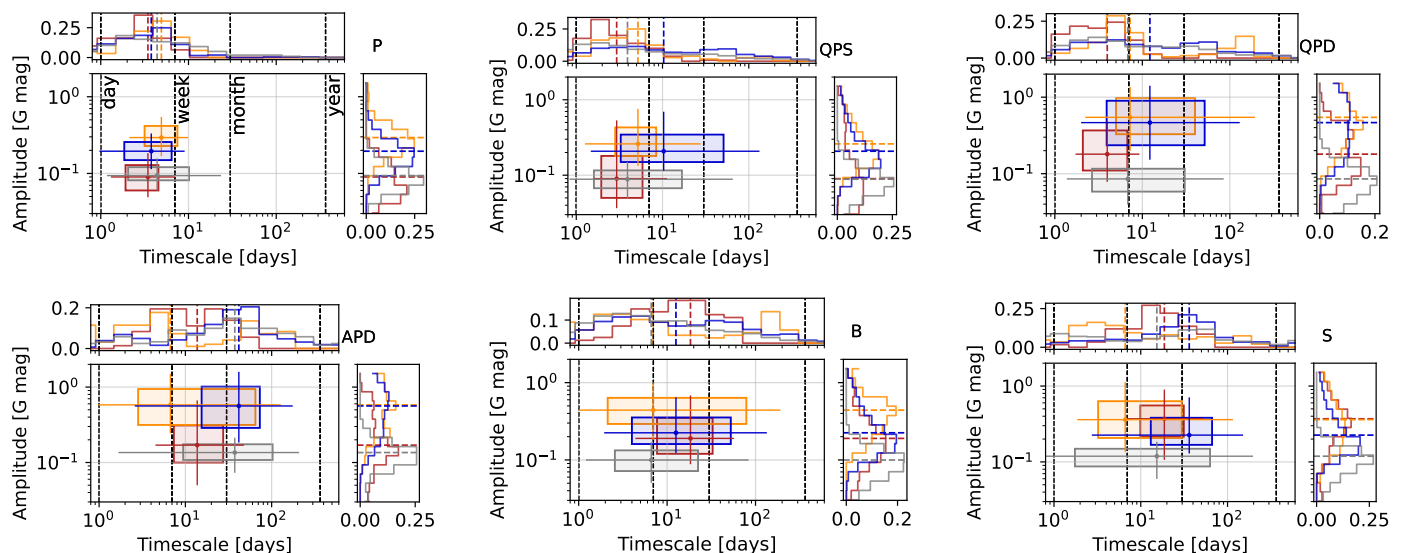


**Fig. 14.** Box plots of timescale-amplitude distribution for six morphology classes based on the Q&M indices. Normalized histogram distributions for each of those quantities are also shown. Our primary sample is in blue, and the secondary in grey. Sources from previous studies with high cadence data (CoRoT, K2) are in red; ground-based studies (ZTF) results are in orange. Coloured dashed lines show the median of the distributions. Black dashed lines show reference timescales. Distributions are shown for Strictly Periodic (P, top left), Quasi-periodic symmetric (QPS, top-middle), Quasi-periodic dippers (QPD, top right), Aperiodic Dippers (APD, bottom left), Bursters (B, bottom-middle); Stochastic (S, bottom-right).

The solar-like variables identified by [Distefano et al. \(2022\)](#) focus on late-type stars, which include some relatively young sources, while being disjoint from the GDR3 YSO sample. This suggests that a certain fraction of young P and QPS variables may be lost to their sample. To quantify sources *lost* to GDR3’s sample of solar-like variables, we further examined the NEMESIS YSO catalogue for the Orion Star Formation Complex ([Roquette et al. 2025](#)) which contains 27 879 YSO candidates. The NEMESIS YSO sample included 5 231 sources in common with Gaia’s YSO sample, of which 111 were classified as P and 2 131 as QPS, and further 152 sources in common with Gaia’s solar-like variables, suggesting that we miss about  $\sim 7\%$  of cool-spot variables. Similarly, EBs are also a subclass of variables in Gaia, with [Mowlavi et al. \(2023\)](#) reporting more than 2 million EB candidates as part of DR3. A similar comparison to the NEMESIS catalogue suggests that our EB-detection rate might be reduced by half.

We also point to survey-to-survey differences in the time span of observations. High-cadence surveys cover between 40 and 80 days of observations, while ZTF surveys cover 800-1 500 days, and GDR3 750-1 000 days. These differences imply that quasiperiodic phenomena at intermediate timescales may be perceived as aperiodic by studies with reduced time span. Moreover, L-variables are defined as sources with timescales larger than 20-40 d in high-cadence studies, 100-250 d in ZTF, we use 350-500 d in the present study. L-variable fractions are thus fully survey-dependent. Even if removed from our class incidence comparison, their impact on the definition of other morphological classes is still worth mentioning. First, L-variables could be operationally defined as aperiodic, since their time scale was not resolvable over the duration of a survey. Although their lack of reliable timescale implies that their Q indices cannot be estimated, their M indices reveal that they would increase class frequencies by 3.8% for B, 8.6% for S, and 5.3% for APDs - thus bringing our class incidence for S and APD variables to levels similar to those of ZTF studies. Second, the timescale limit for the L-variable definition indirectly determines how many folds

are used in the waveform estimation required to derive the Q index. With our threshold of half of the total duration of observations, only one fold is included for sources with the longest timescales, which may lead to over-fitting of estimated waveforms, resulting in deflated Q-indices, and causing aperiodic phenomena to be miss-detected as quasiperiodic.

Some previous studies attributed multiple morphological classes to multi-mode variables (e.g. [Cody & Hillenbrand 2018](#); [Cody et al. 2022](#); [Hillenbrand et al. 2022](#)) also including an additional class, multiperiodic, to account for variables with multiple periods. To improve the comparison of class frequencies with previous studies, in Table 2 we removed sources classified as multiperiodic and adopted the primary morphological class when multiple are reported. Nevertheless, with our focus on the dominant mode of variability, we acknowledge that undetected multi-mode variables in our sample may display inflated Q-indices. Beyond multiple variability mechanisms that occur simultaneously, the longer timespan of surveys like Gaia and ZTF may also facilitate the observation of sources with alternating dominant variability phenomena. For example, this can result in symmetric M-indices derived from light curves that shift from bursting to dipping behaviour (an example is shown in Fig. 20).

Our combined fraction of dipping variables (QPD+APD) is equivalent to the one found in ZTF studies, but smaller than the one found in high-cadence studies. Nevertheless, as already noted, our APD fractions are underestimated due to our definition of L-variables. Furthermore, in Sects. 6.2.3 and 6.2.4 we discuss evidence that our sample of dippers includes a different underlying population of YSOs in comparison to the high-cadence surveys. Similarly, B-variables also include different variability mechanisms, and in Sect. 6.2.5 we discuss evidence that Gaia’s sampling yields the detection of a distinct population of bursting variables in comparison with other surveys.

## 6.2. General properties of Morphological Classes

In this section, each variability morphological class is discussed within the context of its expected physical origins and its typical timescale and amplitude.

### 6.2.1. Strictly Periodic

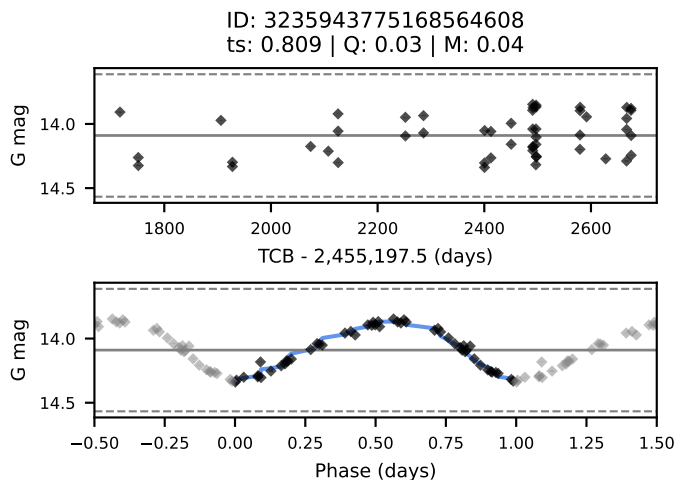


**Fig. 15.** Example of a strictly periodic light-curve (P). *Top*: full G-band light-curve. *Bottom*: phase-folded light-curve. The blue line shows the waveform estimated as part of the Q-index calculation. The gray continuous line shows the average magnitude, and the dashed lines show the  $3\sigma$  variation level.

Strictly periodic variability, P (see Fig. 15), is typically associated with rotational modulation by magnetically induced cool spots at the stellar surface in sources viewed close to edge-on ( $\sim 40\text{--}90^\circ$ ; Cody et al. 2022). From the top-left panel of Fig. 14, the timescale distribution for P sources is consistent across studies and dominated by rotational timescales. The variability amplitude in our primary sample (blue) is higher than that reported in high-cadence surveys (red) but slightly lower than in ZTF studies (orange); the secondary sample (grey) exhibits amplitude levels comparable to those of high-cadence studies. Differences in amplitude distributions can be attributed to selection effects in different surveys. Typically, cool spots have lifetimes ranging from 1 to 50 rotation cycles (Basri et al. 2022). Higher-cadence surveys, which usually span 40 to 80 d, provide excellent phase coverage before significant changes in spot coverage occur. In Gaia, sparse sampling and long-term coverage implies that hundreds of rotation cycles take place before achieving sufficient phase coverage, thus biasing the sample of P sources towards sources with larger and more stable spot coverage (and large amplitudes). In contrast, the higher noise level of ZTF’s ground-based observations allows only the higher-amplitude variables to be detected. As a result, Fig. 14 shows that the ZTF distributions of all classes are shifted toward higher amplitudes compared to other surveys.

The properties of our sample of P-variables support the hypothesis that their variability is primarily driven by rotational modulation linked to relatively stable cool spots. Their average amplitude is among the lowest of all morphological classes, and the ratio between rotation and intermediate timescales (Table 1) shows that this sample is dominated by rotational modulation. P-variables are 82.95% composed of YSOs without evidence of a thick disk or envelope. Furthermore, 86.27% of P-sources with H $\alpha$  information are WTTS.

### 6.2.2. Quasi-periodic Symmetric

As discussed in Sec. 6.1, QPS (see Fig. 16) is the most common morphological class among our entire sample. Multiple physical origins have been proposed for QPS. Although generally linked to rotational modulation of stellar spots, high-amplitude QPS have been tentatively associated with variability caused by large hot spots induced by accretion, in combination with underlying lower-amplitude accretion variation (Venuti et al. 2015; Cody & Hillenbrand 2018), while low-amplitude QPS are thought to originate from changes of cool spot coverage due to magnetic activity (Cody et al. 2022). Considering that cool spots are the only variability driver expected in diskless sources and that disk-bearing and actively accreting sources are likely to exhibit accretion-induced hot spots, this view is generally supported by our sample. We find that the average distribution of amplitudes is lower for diskless and thin-disk QPS (0.11 mag) compared to sources with envelope or thick disk (0.30). Similar differences are found when comparing the amplitudes of the WTTS QPS (0.11) with the CTTS QPS (0.36). The same trend is verified by comparing our primary and secondary samples, where the CTTS frequency varies from 36.6% to 6.1%.

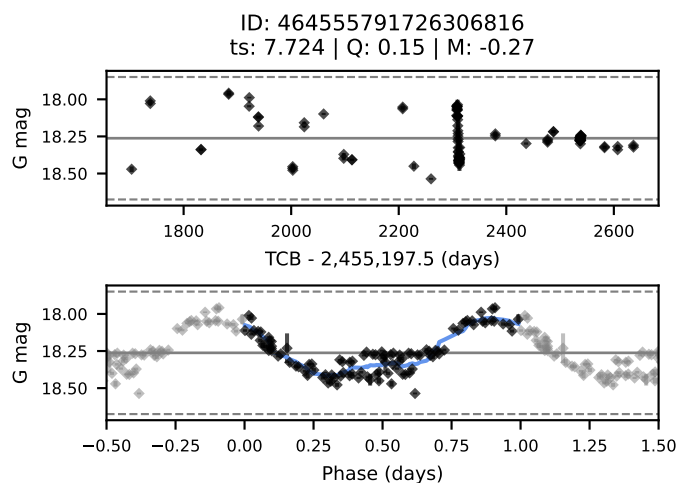


**Fig. 16.** Example of quasi-periodic symmetric (QPS) light-curve. General plot description as in Fig. 15.

Our QPS-variables include a population of sources with intermediate timescales, which has not been found in previous studies. Fig. 14 shows that for the primary sample, the timescale distribution is bimodal, with 1.3 times as many rotation timescales as intermediate ones. A comparison of their Q-index distributions reveals significant differences (with KS test support), where the rotational-timescale QPS are shifted toward higher periodicity with an average Q of 0.34 compared to 0.44 for intermediate-timescale QPS. Visual inspection of intermediate-timescale QPS light curves revealed that many of these sources have limited phase coverage when folded to their characteristic timescale. This limitation is inherent in surveys with sparse sampling as Gaia, where some phase-folded light curves with poor phase coverage include large gaps with no data. These gaps, by turn, bring us to the limits of the methodology for waveform estimation, causing waveforms to be over-fit to only a fraction of the phase, artificially shifting Q-indices towards smaller values and causing miss-detection of aperiodic sources as quasi-periodic. With Gaia’s scanning law, the timescales that yield gaps in phase coverage vary with sky position, making modelling and masking these timescales from our analysis un-

practical. To mitigate this issue, further studies should consider the complementation of Q&M-analysis with an additional variability metrics sensitive to the degree of phase coverage as part of the procedure for the derivation of the Q index (e.g. [Saunders et al. 2006](#)). We also considered adjusting the quasi-periodic/aperiodic Q-index threshold to mitigate this effect, but verified that a lower Q-index limit would result in reliable quasi-periodic light-curves with rotation timescales being misclassified as aperiodic.

### 6.2.3. Quasi-periodic Dippers

QPD light curves (see Fig. 17) are often associated with the phenomenology of AA Tauri variables ([Bouvier et al. 1999](#)). In such cases, a misalignment between the rotation and magnetic field axes yields the formation of wraps, with disk material lifted above the disk's mid-plane and close to the co-rotation radius, introducing quasi-periodic occultations at rotational timescales in systems observed close to edge-on ([Romanova et al. 2013](#); [McGinnis et al. 2015](#)). Among the primary sample, 62.09% of QPD have an inner disk, and 40.60% have evidence of ongoing accretion (CTTS classification), supporting the association of this class with physical phenomenology related to the presence of a disk and ongoing accretion. However, a direct association of these with the AA Tau prototype is hampered by two factors.

Firstly, we noted that a fraction of our low-amplitude QPDs may be misclassified QPS light-curves. About half of our QPDs are in the secondary sample, which shows a much lower disk frequency (13.71%), and even lower CTTS frequency (4.47%), with both Q and M distributions shifted in relation to the primary sample towards more symmetric M-indices and more periodic Q-indices. Fig. 14 shows that these have systematically lower amplitudes than QPD from high-cadence surveys. The M-index distribution for the secondary QPD sample peaks close to the threshold for dipper selection with 90% of the M-indices for this sample below the median value for the primary QPD sample. Additionally, although statistically different in shape, the distributions of amplitudes and Q-index for the secondary QPD and secondary QPS samples have similar averages and standard deviations, as well as similar disk and CTTS frequency. Finally, visual examination of the light curves also suggested that a higher M-index threshold might be necessary to enhance the purity of the dipper variable samples, where a reviewed threshold would identify a large fraction of secondary QPD as QPS.

Secondly, because of Gaia's much longer observation time span, QPDs may be sensitive to other dimming variables beyond AA Tau. Fig. 14 reveals a bimodal distribution for QPDs, with  $\sim 35\%$  of QPDs showing intermediate timescales. This contradicts the predictions of the AA Tau phenomenology, where the occulting material is anticipated to be near the co-rotation radius. The primary sample of QPDs with intermediate timescales shows high disk and CTTS frequencies (65.09, and 47.35%), suggesting a physical origin also associated with the presence of a disk and ongoing accretion. Statistical tests for distribution shape, mean and variance differences for the distributions of Q-indices and amplitude support the hypothesis that our primary QPD sample is composed of two distinct populations of variables with rotation and intermediate timescale, where the rotation timescale QPDs have lower amplitude on average (0.29 mag) and are more periodic (lower Q), while the intermediate timescale QPDs tend to have larger amplitude on average (0.44 mag) and reduced periodicity in comparison. We note that this second population of intermediate-timescale QPDs is also

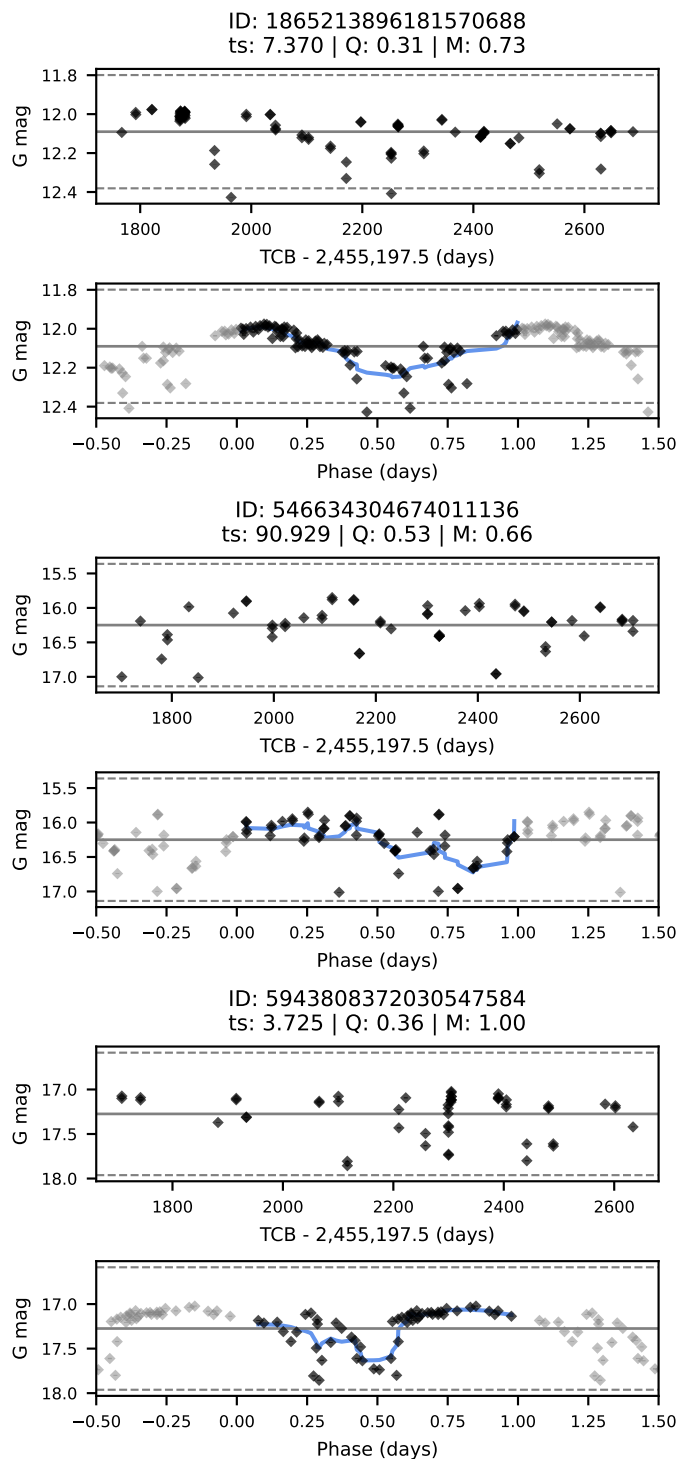


**Fig. 17.** Examples of quasi-periodic dipper light curves at rotational timescales (Top and Bottom) and intermediate timescale (middle). General plot description as in Fig. 15.

present in the ZTF sample, which has a timespan close to Gaia's, suggesting that this second type of QPDs is absent from high-cadence surveys due to their limited total timespan.

While QPDs at rotational timescales can be associated with AA Tau type variability, QPD with intermediate timescales could be related to occultation by disk-material located farther away than the inner disk. One possible prototype for this variability behaviour could be the young star RW Aur ([Cabrit et al. 2006](#); [Facchini et al. 2016](#)). A proposed phenomenological explanation

for the fading of RW Aur would be a tidally truncated disk in which a flyby removed the outer part of the disk, leaving a tidally disrupted 'arm' that induces occultations of stellar light when observed from moderate viewing angles (e.g. [Rodríguez et al. 2013](#)). We note that although RW Aur is best known for its 2 mag deep fading events in 2010 and 2014, lower amplitude variability could be expected under the same phenomenology (e.g. [Fischer et al. 2023](#)). A different possible phenomenon could be disk instabilities as a trigger of dense disk winds responsible for enhancing line-of-sight extinction above the disk mid-plane, which, due to their radial location, would cause rotational modulation at longer timescales (e.g. [Bouvier et al. 2013](#)). Further constraints on the colour behaviour during dipping features could help further probing of QPD.

#### 6.2.4. Aperiodic Dippers

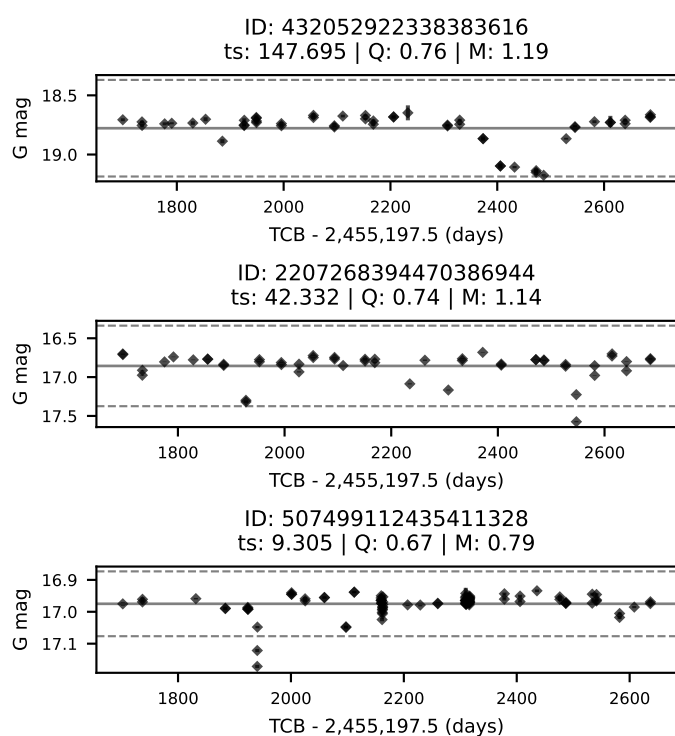


**Fig. 18.** Examples of Aperiodic Dipper light-curves. General plot description as in Fig. 15.

APD-variables (see Fig. 18) have the highest inner disk and CTTS frequencies (56.94 and 39.64%), pointing to an association of their observed variability with the star-disk interaction process. Previous studies have also linked APDs to the physical phenomenology of AA Tau. However, while QPDs require star-disk systems that undergo stable accretion to allow dust to be lifted above the disk midplane long enough for the occultations to be observed as quasiperiodic, in APDs, an unstable accretion regime will instead result in stochastically distributed aperiodic dippers through the light curve ([Kulkarni & Romanova 2008](#); [McGinnis et al. 2015](#)). Nevertheless, material occulting the star is still expected to be at around the co-rotation radius, thus aperiodic occultation features are still expected to have durations around rotational timescales. In contrast, Tables 1 and Fig. 14 reveal that APDs show intermediate timescales 2.26 times more often than rotational ones.

We note that a meaningful interpretation of aperiodic timescales can be tricky. Fig. 14 shows that APDs from high-cadence surveys have timescales between a week and a month, with these surveys being limited to a time span of 40-80 days. May their APDs be in reality an undersampled quasiperiodic phenomenon occurring over timescales longer than their timespan, these will be detected as quasiperiodic by surveys like Gaia or ZTF, which explains the population of intermediate timescales among our QPDs, and the reduced population of rotation timescales in our primary APDs sample. Second, most aperiodic light curves had their timescale determined by the SF in Sect. 4.2.2. SF aperiodic timescales measure the time it takes for the dominant variability feature in the light curve to reach its maximum amplitude, thus reflecting the duration of the variability feature, rather than the frequency of occurrence of variability over the span of observations. For example, the bottom panel of Fig. 18 shows an APD light curve potentially linked to the AA Tau phenomena, where the 9.3 d derived aperiodic timescale reflects the time to reach the maximum amplitude (0.24 mag) in the main dip visible in the light curve. In the top panel of the same figure, we show a second example where the timescale of 147.7 days reflects half of the duration of a main fading event with amplitude 0.53 mag. Combined with the large amplitudes found among our primary sample of APDs, the large disk and CTTS frequencies and large aperiodic timescales support the suggestions that beyond AA Tau-like light curves, APDs at intermediate timescales may be a population of moderate-amplitude RW Aur fading light curves (e.g. [Petrov et al. 2015](#)).

#### 6.2.5. Bursters

B-variables were previously associated with high levels of accretion based on correlations with various accretion proxies, from UV excess to variability in colour behaviour and  $H\alpha$  ([Stauffer et al. 2014](#); [Cody et al. 2017](#); [Venuti et al. 2021](#); [Hillenbrand et al. 2022](#)). In our sample, this association with star-disk-interaction phenomenology is only supported for sources in our primary B sample, for which the inner disk and CTTS frequency were 45.18% and 45.49%, while for the secondary sample these are 12.22 and 7.04% respectively.

As defined by [Cody et al. \(2014\)](#), the B class might constitute a family of bursting behaviours, rather than relating to a single physical mechanism. In a study focused solely on B-variability, [Cody et al. \(2017\)](#) finds varied B behaviour, with some sources showing a continuous series of bursts, while others presenting short-lived burst episodes on top of underlying irregular variability (see also [Venuti et al. 2021](#)). This family of prototypical B behaviour is verified among our primary B sample, and illustrated in Fig. 19, where we show examples of isolated bursts, including both short-lived (GDR3 510735868513196160) and longer-lived bursts (GDR3 6236134222781410944). Fig. 19 also includes an example of a quasi-periodic B variable with intermediate timescale, GDR3 2069894002944444928, which may be related to the phenomenology behind the DQ Tau system ([Tofflemire et al. 2017](#)), where two stars orbit each other in a highly eccentric orbit and their magnetic interaction with circumbinary and circumstellar material yields enhanced accretion near periastron, resulting in the observation of regular bursts.

Following the discussion on outlier removal in Sect. 3.4 and App. A.3, we note that Gaia's sparse cadence is expected to yield an under-detection of variables with short-lived bursts. As reported by [Cody et al. \(2017\)](#), only 1 burst out of 29 monitored with high-cadence K2 light curves showed burst durations longer than 10 days. If observed by Gaia, such a sample would likely

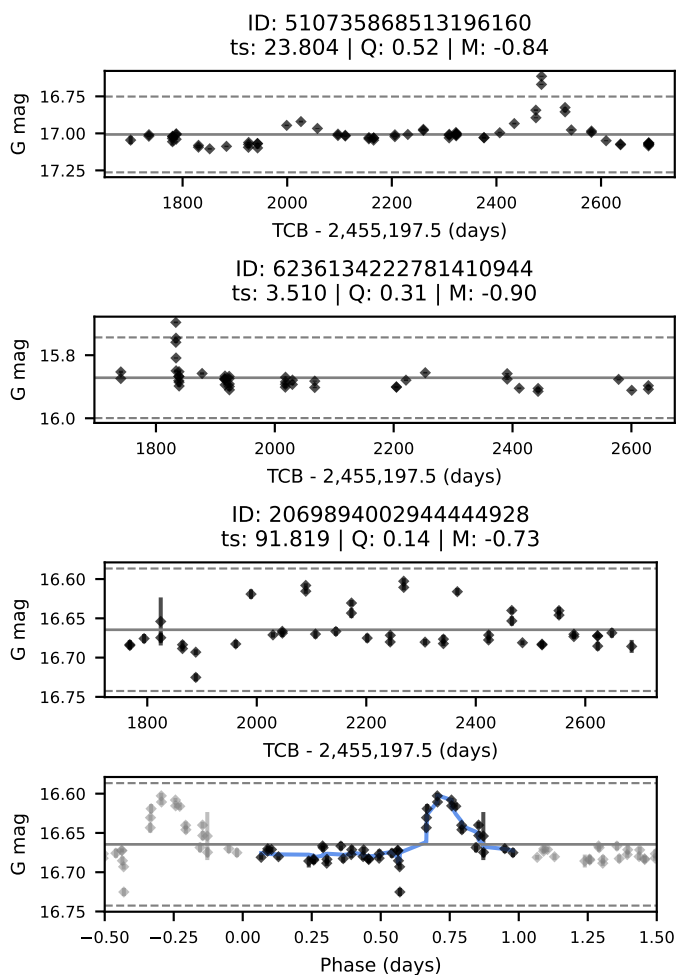


**Fig. 19.** Examples of bursting light curves. *Top*: Aperiodic B variable with intermediate duration bursting feature. *middle*: Example of a short duration burst coinciding with a cusp. *Bottom*: Full and phase-folded light curves for a quasi-periodic burster. General plot description as in Fig. 15

have burst events ruled out as outliers, unless the bursting feature coincides with a cusp, as in the case of a short-lived burst variable GDR3 6236134222781410944 shown in Fig. 19.

Finally, we did not find examples of extreme burst events, such as a FUor or EXors, among our sample of B sources. However, we verified the existence of some sharp long-term bursts among our long-trend variables (see the top panel of Fig. 22).

### 6.2.6. Stochastics

S variables (Fig. 20), are dominated by irregular variability without detectable periodicity or a clear preference for bursting or dimming behaviour. Fig. 14 shows that even our primary sample shows systematically lower amplitudes compared to previous studies. Previous high-cadence surveys associated S-variables with a combination of the erratic routine variability introduced by accretion combined with viewing angles close to face-on, which hindered the rotational modulation of accretion-induced variability (Stauffer et al. 2016). This scenario is supported by our main S-sample, which has inner disk and CTTS frequencies of 43.26 and 49.04%, respectively, along 2.26 times as many intermediate timescales as rotational ones. However, visual inspection of S light curves shows that a fraction of those are multi-

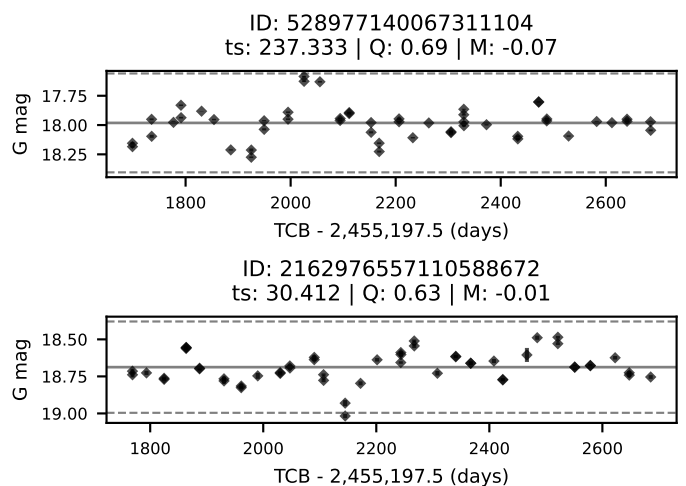


**Fig. 20.** Examples of stochastic light curves. *Top*: typical S variable with no preference for bursting or dipping. *Bottom*: S variable with alternating behaviour between dipping and bursting. General plot description as in Fig. 15

mode variables with alternating bursting and dipping behaviour across the observed time (see Fig. 20 bottom panel). In contrast, our secondary sample has very low inner disk and CTTS frequency (18, and 7.36%), with a wide spread of timescales and no clear preference for rotational or intermediate timescales. However, when disaggregated by amplitude, this sample reveals an excess of sources with low-amplitude (below 0.1 mag) fast rotation timescale (below 5 days), which may suggest a link between this sample and cool spot dominated light curves close to Gaia’s detection limit.

### 6.2.7. Eclipsing binaries

The EB class in Cody et al. (2014) targeted prototypical eclipsing binary light curves with strictly periodic asymmetric light curves. We found 129 EB sources. A search for counterparts within the Simbad Database (Wenger et al. 2000) reveals that only 4 of our EB sources were previously identified as such in the literature. We note that although sources classified as EB generally followed the prototype of strictly periodic eclipses, our automated method for timescale derivation with the GLS (Sect. 4.2.1) tends to detect harmonics of the true period as the best timescale. We show two examples of EB light curves in Fig. 21, where in both cases the GLS returned half of the true period as the best timescale. In the case of the source GDR3 5414630399235694976 (top plots), secondary and primary eclipses are relatively similar in depth with the waveform estimated based on the biased timescale representing the true waveform relatively well and yielding a very low Q-value. However, in cases like the source GDR3 2019728853698920704 (bottom plots), as the secondary eclipse is much shallower, waveform estimation based on the harmonic of the true timescale inflates Q values, resulting in the miss-classification of the source as a QPD.

### 6.2.8. Long-trends

Although the L-variables do not have a Q-index (because the timescale was too large to allow a relevant waveform to be derived from the phase-folded curve), we still computed their M-index. In the primary sample, 21% Ls have bursting behaviour

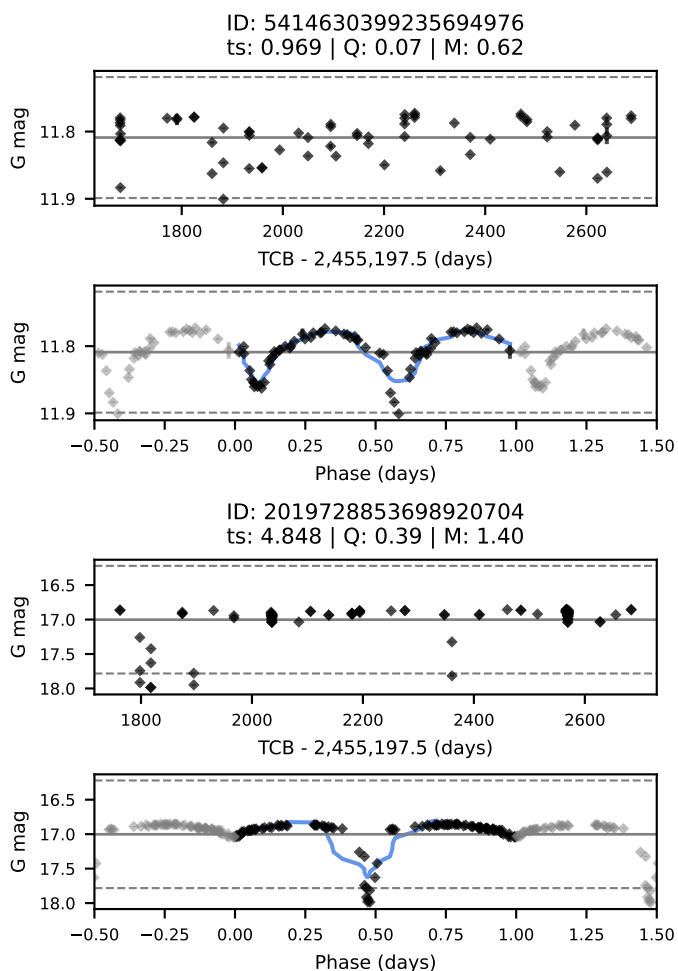


**Fig. 21.** *Top two panels:* Example of an eclipsing binary light curve. *Bottom panels:* Example of an eclipsing binary light curve misclassified as QPD due to timescale detection of harmonic of the true period; We note that in both cases, the timescale derived by the GLS method (ts) was a harmonic of the true period. Phase-folded light-curves shown here account for that by phase-folding sources to twice the GLS timescale. General plot description as in Fig. 15

and 30% have dipping behaviour. For the secondary sample, 21% Ls have bursting behaviour, and 26% have dipping behaviour. Ls tend to have larger amplitudes than the other classes, which is expected since there is an empirical correlation between the timescale of an event and its amplitude (See Fig. 3 of Fischer et al. 2023).

### 6.3. Comparison across surveys

To further investigate the consistency of Q and M indices across different surveys, we cross-matched our variable sample with previous Q&M studies using K2 (Cody et al. 2022) and ZTF (Hillenbrand et al. 2022; Wang et al. 2023; Jiang & Hillenbrand 2024). Figs. 23 and 24 show examples of light curves of sources with observations in multiple surveys. We emphasise that none of the light curves in question included common seasons of observations.

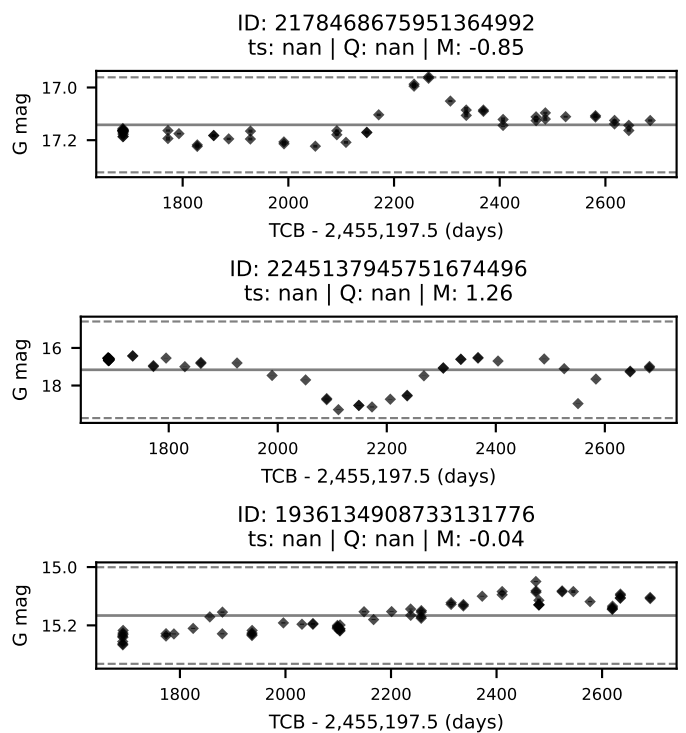


**Fig. 22.** Long-trends light-curves for a bursting (top), dipping (middle) and symmetric (bottom) source. General plot description as in Fig. 15

### 6.3.1. High-cadence space-based surveys

We found only 13 sources in common between our variable sample and the sources observed by Cody et al. (2022) with K2 in Taurus (see Fig. 23). Hence, we limit our comparison to a qualitative discussion. Since K2 and GDR3 have very different cadences and timespans, our comparison focuses on their M-index behaviour, where classification was considered equivalent if the source was detected as dipping, symmetric or bursting in both surveys. Although variability amplitudes were generally consistent across surveys, Q&M-indices often had large enough differences to produce distinct morphological classes.

Of the three symmetric sources in K2, only one was also symmetric in GDR3, while the others were dipping. However, since these surveys cover different seasons of observation, it is impossible to infer whether discrepant classifications result from a change in dominant variability mode or the result of different cadences of observations. Three B-variables in K2 were also B in GDR3. One of these sources is GDR3 3409319239697943296 (Fig. 23), which, although bursting in both surveys, was quasiperiodic in our study and aperiodic when observed by K2. Of the four dipping variables in K2, three were also dipping in GDR3. Cody et al. (2022) searched for multiple variability modes by computing Q&M twice: first on the original light curve and then on the residual data. Two out of three multimode sources in common with GDR3 have one of their morphological classes matched to GDR3. An example is shown in Fig. 23, where the QPD source GDR3 3406128761895775872 was attributed to the QPS and APD classes in the K2 analysis.

### 6.3.2. Comparison with ZTF

ZTF light curves have a similar duration to GDR3, but are noisier due to ground-based observations. We found 165 sources in common with ZTF studies. Of these, 25 sources were sorted as

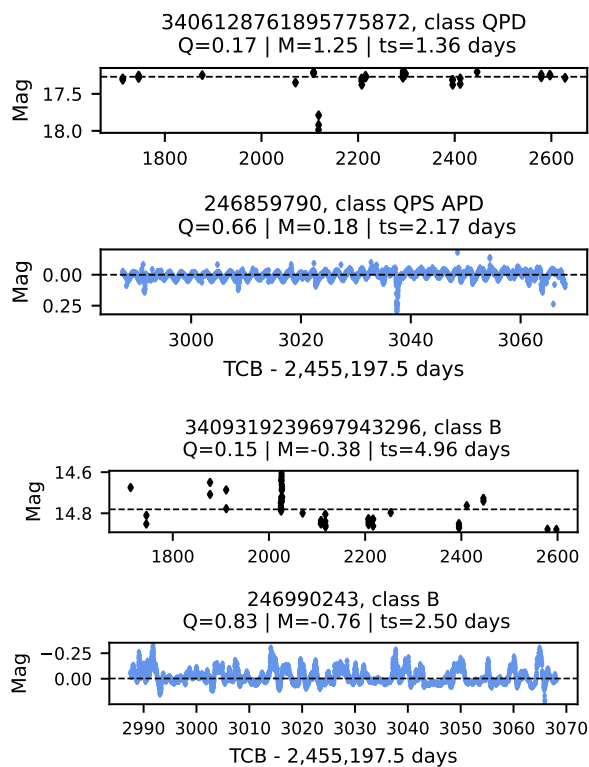


**Fig. 23.** Light curves comparison between GDR3 (top) and K2 (bottom). Horizontal black dashed lines show the median magnitude.

L by our method, thus having no Q-index. Two example light curves are displayed in Fig. 24. GDR3 2067026678480142464, on the top panel, shows a similar behaviour in both surveys. Although it was classified as a long-trend by us, its M-index implies bursting behaviour. GDR3 M-index is slightly shifted towards more symmetric compared to ZTF. GDR3 216701033028221312 (bottom panel) has a similar behaviour in both surveys, with matching timescales. However, the dispersion is considerably more significant in the ZTF data than in GDR3, resulting in a higher Q-index value for ZTF. Additionally, the ZTF light curve contains significantly more data points, contributing to its more symmetric behaviour compared to GDR3.

Fig. 25 shows the Q-M diagrams for each of the GDR3 classes (except L), with both the GDR3 and ZTF results scattered. At a population level, results between the two surveys are relatively consistent, especially in terms of light-curve symmetry. There were very few cases where variables were detected in radically different behaviours, for example, switching from bursts to dips. For periodic and quasi-periodic sources, we find that differences in derived timescales were either due to harmonics, or could be explained by the 1-day aliasing caused by ZTF's ground-based observations. For aperiodic sources, the timescales were significantly different. However, these can be traced back to different methodologies used for the aperiodic timescale derivation. Given the different Q-index thresholds adopted in ZTF surveys, most QPS variables in Gaia were also QPS in ZTF. A few dippers in ZTF were detected as QPS or S-variables in Gaia, although we note that these are generally close to the M-threshold in our study. Most dippers (QPDs or APDs) in Gaia were also dippers in ZTF. Although a fraction of Gaia's B-variables are recovered by ZTF, most bursts in Gaia are detected as symmetric in ZTF. Nevertheless, we note that because of their lower cadence,

both Gaia and ZTF are expected to be inefficient in detecting bursts.

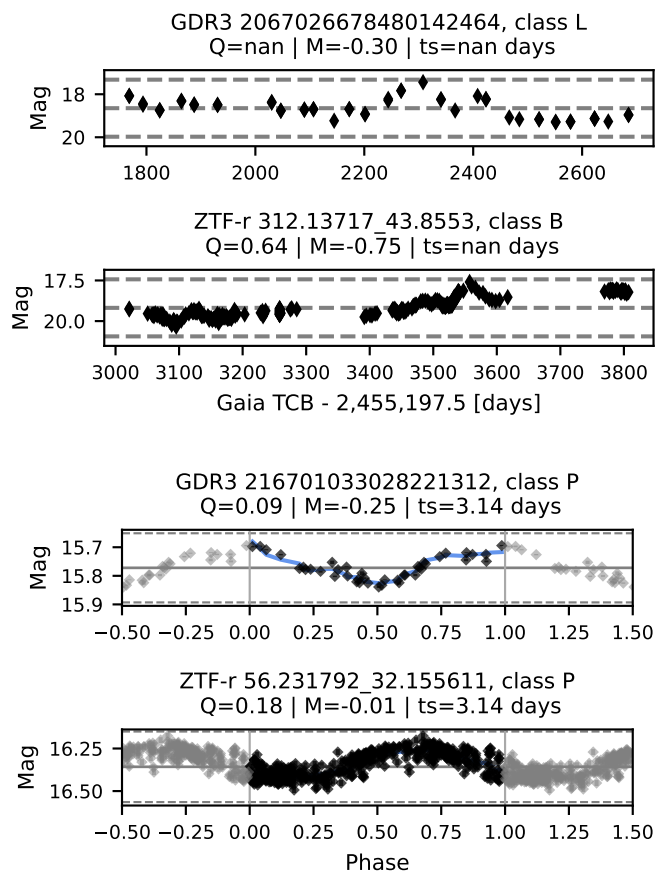


**Fig. 24.** Light curves comparison between GDR3 (top) and ZTF (bottom). Dashed lines show average and  $3\sigma$  values. The periodic source (bottom) is phase-folded to the best timescale in each survey.

## 7. Summary and conclusions

In this paper, we presented the results of a pilot study employing the asymmetry and periodicity variability metrics to characterise an all-sky sample of YSO candidates based on their G-band photometric variability observed with Gaia. We have adapted the methodology behind the Q&M-indices for application to Gaia's long-term sparse light curves. This methodology was further developed into an automated workflow for managing large datasets. Starting from the sample of 79 375 variables identified in GDR3 as YSO candidates based on their variability, we pre-processed sources to filter for a low number of epochs, remove contaminants and identify sources likely affected by spurious instrumental variability. Based on a sample of 28 179 sources, we inferred characteristic timescales of variability considering both the possibility of periodic and aperiodic variability. The timescale distribution revealed a bimodality of rotational and intermediate timescales, with the former showing slightly lower variability amplitudes on average than the latter. Rotational timescales were more frequent for sources with enhanced periodicity and intermediate timescales for aperiodic sources. We could successfully derive Q&M indices for 23 213 sources. We complemented our analysis with observations of H $\alpha$  as a proxy of ongoing accretion and  $\alpha_{IR}$  as a proxy of the pres-

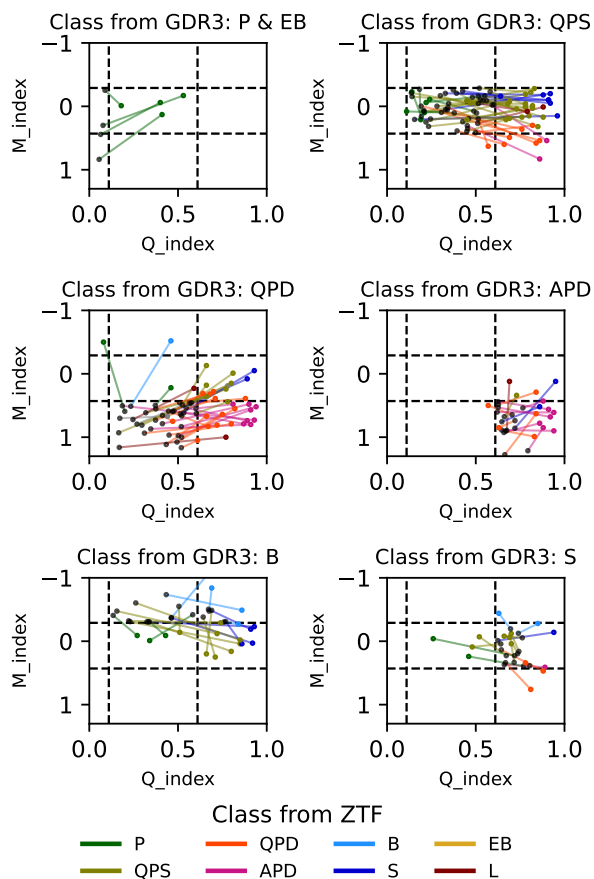


**Fig. 25.** Q-M diagrams with GDR3 (black dots) and ZTF (colour dots). The subplots shows the sources from each morphological class as determined in our GDR3 study. Ps and EBs are displayed on the same subplot. The colours indicate the class from Hillenbrand et al. (2022); Wang et al. (2023); Jiang & Hillenbrand (2024), derived from ZTF light curves. ZTF classes were not made based on the Q-M distribution but determined by eye. The black dashed lines show the threshold we applied to class our samples.

ence of circumstellar material and the evolution stage of YSOs. We found that WTTS diskless sources tend to show more periodic and symmetric variability, while CTTS and WTTS disk-bearing sources tend to be more asymmetric and less periodic.

We used the derived Q&M indices to sort sources into one of six variability morphology classes: Strictly Periodic, Quasiperiodic Symmetric, Stochastic, Quasiperiodic Dipper, Aperiodic Dipper, Burst, or Eclipsing binary. 4966 additional sources had detected timescales longer than half of the total observed time and were classified as Long-trend, with only M-index derived. The subsamples in each of these classes were further examined in terms of Q&M-indices, variability amplitudes, timescales, and accretion and disk proxies with possible links to well-known variability mechanisms discussed. This examination revealed a wider variety of variability behaviour than previous studies, which we attribute to Gaia’s longer timespan. We found sources displaying the usual variability caused by rotational modulation by magnetically induced spots, or accretion induced hot spots, and both bursting and dipping behaviour at rotational timescales, likely linked to star-disk-interaction. Moreover, we found a relevant fraction of sources showing dipping and bursting behaviour at intermediate timescale, which we tentatively linked to the phe-

nomenology behind RW Aur fades, and DQ Tau-type bursting variability.

We qualitatively compared our Q&M-based results to previous studies, considering both the results of high-cadence surveys (CoRoT and K2) and ground-based surveys (ZTF) and including discussion at the individual and population levels. Although large survey-to-survey differences are found, M-index trends seem generally consistent. When considering survey-specific biases (caused by cadence, timespan, precision and age), we found that the differences in the incidence of morphological classes across surveys can be explained. We note a lack of available observed datasets with common sources observed by Gaia and high-cadence surveys, which would allow us to probe the appropriateness of Q&M thresholds for classification across surveys. Future studies should consider assessing the influence of survey-to-survey variations on these thresholds based on simulated data. Finally, Gaia DR4 will allow us to expand these results to an even broader all-sky coverage, thanks to the longer timespan of observations and improved calibration.

*Acknowledgements.* We acknowledge funding from the European Union’s Horizon 2020 research and innovation program (grant agreement No.101004141, NEMESIS). G.M. acknowledges support from the János Bolyai Research Scholarship of the Hungarian Academy of Sciences. We thank Berry Holl for helpful discussions on the use of Gaia DR3 data, Ann-Marie Cody and Laura Venuti for exchanges about the implementation of the Asymmetry and Periodicity metrics. This research was also supported by the International Space Science Institute (ISSI) in Bern, through ISSI International Team project 521 selected in 2021, Revisiting Star Formation in the Era of Big Data (<https://teams.issibern.ch/starformation/>) This work made use of Astropy (Astropy Collaboration et al. 2013, 2018, 2022), Scikit-learn: Machine Learning in Python (Pedregosa et al. 2011), Pandas (pandas development team 2020), Numpy (Harris et al. 2020), and Matplotlib (Hunter 2007). This work has made use of data from the European Space Agency (ESA) mission *Gaia* (<https://www.cosmos.esa.int/gaia>), processed by the *Gaia* Data Processing and Analysis Consortium (DPAC, <https://www.cosmos.esa.int/web/gaia/dpac/consortium>). Funding for the DPAC has been provided by national institutions, in particular the institutions participating in the *Gaia* Multilateral Agreement. This research has made use of the SIMBAD database, operated at CDS, Strasbourg, France

## References

- Alencar, S. H. P., Teixeira, P. S., Guimaraes, M. M., et al. 2010, *A&A*, 519, A88  
 Andre, P., Ward-Thompson, D., & Barsony, M. 1993, *ApJ*, 406, 122  
 Astropy Collaboration, Price-Whelan, A. M., Lim, P. L., et al. 2022, *ApJ*, 935, 167  
 Astropy Collaboration, Price-Whelan, A. M., Sipőcz, B. M., et al. 2018, *AJ*, 156, 123  
 Astropy Collaboration, Robitaille, T. P., Tollerud, E. J., et al. 2013, *A&A*, 558, A33  
 Auvergne, M., Bodin, P., Boissard, L., et al. 2009, *A&A*, 506, 411  
 Baluev, R. V. 2008, *MNRAS*, 385, 1279  
 Barrado y Navascués, D. & Martín, E. L. 2003, *AJ*, 126, 2997  
 Basri, G., Streichenberger, T., McWard, C., et al. 2022, *ApJ*, 924, 31  
 Bouvier, J., Chelli, A., Allain, S., et al. 1999, *A&A*, 349, 619  
 Bouvier, J., Grankin, K., Ellerbroek, L. E., Bouy, H., & Barrado, D. 2013, *A&A*, 557, A77  
 Bredall, J. W., Shappee, B. J., Gaidos, E., et al. 2020, *MNRAS*, 496, 3257  
 Buder, S., Kos, J., Wang, E. X., et al. 2024, arXiv e-prints, arXiv:2409.19858  
 Cabrit, S., Pety, J., Pesenti, N., & Dougados, C. 2006, *A&A*, 452, 897  
 Carpenter, J. M., Hillenbrand, L. A., & Skrutskie, M. F. 2001, *AJ*, 121, 3160  
 Cody, A. M. & Hillenbrand, L. A. 2018, *The Astronomical Journal*, 156, 71  
 Cody, A. M., Hillenbrand, L. A., David, T. J., et al. 2017, *ApJ*, 836, 41  
 Cody, A. M., Hillenbrand, L. A., & Rebull, L. M. 2022, *The Astronomical Journal*, 163, 212  
 Cody, A. M., Stauffer, J., Baglin, A., et al. 2014, *AJ*, 147, 82  
 Creevey, O. L., Sordo, R., Pailler, F., et al. 2023, *A&A*, 674, A26  
 De Angeli, F., Weiler, M., Montegriffo, P., et al. 2023, *A&A*, 674, A2  
 Dembinski, H. & et al., P. O. 2020  
 Distefano, E., Lanzafame, A. C., Brugaletta, E., et al. 2022, arXiv e-prints, arXiv:2206.05500  
 Evans, D. W., Eyer, L., Busso, G., et al. 2023, *A&A*, 674, A4

- Eyer, L., Audard, M., Holl, B., et al. 2023, *A&A*, 674, A13
- Eyer, L. & Genton, M. G. 1999, *A&AS*, 136, 421
- Facchini, S., Manara, C. F., Schneider, P. C., et al. 2016, *A&A*, 596, A38
- Findeisen, K., Cody, A. M., & Hillenbrand, L. 2015, *ApJ*, 798, 89
- Fischer, W. J., Hillenbrand, L. A., Herczeg, G. J., et al. 2023, in *Astronomical Society of the Pacific Conference Series*, Vol. 534, *Protostars and Planets VII*, ed. S. Inutsuka, Y. Aikawa, T. Muto, K. Tomida, & M. Tamura, 355
- Gaia Collaboration, Bailer-Jones, C. A. L., Teyssier, D., et al. 2023a, *A&A*, 674, A41
- Gaia Collaboration, Prusti, T., de Bruijne, J. H. J., et al. 2016, *A&A*, 595, A1
- Gaia Collaboration, Vallenari, A., Brown, A. G. A., et al. 2023b, *A&A*, 674, A1
- Gaia ESA Archive. , official webpage, <https://gea.esac.esa.int/archive/>
- Genova, F., Egret, D., Bienaymé, O., et al. 2000, *A&AS*, 143, 1
- Gilmore, G., Randich, S., Worley, C. C., et al. 2022, *A&A*, 666, A120
- Ginsburg, A., Sipőcz, B. M., Brasseur, C. E., et al. 2019, *AJ*, 157, 98
- Greene, T. P., Wilking, B. A., Andre, P., Young, E. T., & Lada, C. J. 1994, *ApJ*, 434, 614
- Harris, C. R., Millman, K. J., van der Walt, S. J., et al. 2020, *Nature*, 585, 357
- Herbst, W., Herbst, D. K., Grossman, E. J., & Weinstein, D. 1994, *AJ*, 108, 1906
- Hillenbrand, L. A., Kiker, T. J., Gee, M., et al. 2022, *AJ*, 163, 263
- Holl, B., Fabricius, C., Portell, J., et al. 2023, *A&A*, 674, A25
- Hourihane, A., François, P., Worley, C. C., et al. 2023, *A&A*, 676, A129
- Hughes, P. A., Aller, H. D., & Aller, M. F. 1992, *ApJ*, 396, 469
- Hunter, J. D. 2007, *Computing in Science & Engineering*, 9, 90
- James, F. & Roos, M. 1975, *Comput. Phys. Commun.*, 10, 343
- Jiang, S. D. & Hillenbrand, L. A. 2024, *AJ*, 167, 221
- Joy, A. H. 1945, *ApJ*, 102, 168
- Kozłowski, S. 2016, *ApJ*, 826, 118
- Kulkarni, A. K. & Romanova, M. M. 2008, *MNRAS*, 386, 673
- Lada, C. J. 1987, in *Star Forming Regions*, ed. M. Peimbert & J. Jugaku, Vol. 115, 1
- Lakeland, B. & Naylor, T. 2022, in *The 21st Cambridge Workshop on Cool Stars, Stellar Systems, and the Sun*, Cambridge Workshop on Cool Stars, Stellar Systems, and the Sun, 111
- Lomb, N. R. 1976, *Ap&SS*, 39, 447
- Marton, G., Abrahám, P., Rimoldini, L., et al. 2023, *A&A*, 674, A21
- Masci, F. J., Laher, R. R., Rusholme, B., et al. 2019, *PASP*, 131, 018003
- McGinnis, P. T., Alencar, S. H. P., Guimarães, M. M., et al. 2015, *A&A*, 577, A11
- Morales-Calderón, M., Stauffer, J. R., Hillenbrand, L. A., et al. 2011, *ApJ*, 733, 50
- Mowlavi, N., Holl, B., Lecoœur-Taïbi, I., et al. 2023, *A&A*, 674, A16
- Ochsenbein, F., Bauer, P., & Marcout, J. 2000, *A&AS*, 143, 23
- Ordenes-Huanca, C., Zoccali, M., Bayo, A., et al. 2024, *MNRAS*, 533, 841
- pandas development team, T. 2020, *pandas-dev/pandas: Pandas*
- Pecaut, M. J. & Mamajek, E. E. 2013, *ApJS*, 208, 9
- Pedregosa, F., Varoquaux, G., Gramfort, A., et al. 2011, *Journal of Machine Learning Research*, 12, 2825
- Petrov, P. P., Gahm, G. F., Djupvik, A. A., et al. 2015, *A&A*, 577, A73
- Pettersson, B., Armond, T., & Reipurth, B. 2014, *A&A*, 570, A30
- Randich, S., Gilmore, G., Magrini, L., et al. 2022, *A&A*, 666, A121
- Rimoldini, L., Holl, B., Gavras, P., et al. 2023, *A&A*, 674, A14
- Rodríguez, J. E., Pepper, J., Stassun, K. G., et al. 2013, *AJ*, 146, 112
- Roelens, M., Eyer, L., Mowlavi, N., et al. 2017, *MNRAS*, 472, 3230
- Romanova, M. M., Ustyugova, G. V., Koldoba, A. V., & Lovelace, R. V. E. 2013, *MNRAS*, 430, 699
- Roquette, J., Alencar, S. H. P., Bouvier, J., Guarcello, M. G., & Reipurth, B. 2020, *A&A*, 640, A128
- Roquette, J., Audard, M., Hernandez, D., et al. 2025, *arXiv e-prints*, arXiv:2501.08486
- Saunders, E. S., Naylor, T., & Allan, A. 2006, *Astronomische Nachrichten*, 327, 783
- Savitzky, A. & Golay, M. J. E. 1964, *Analytical Chemistry*, 36, 1627
- Scargle, J. D. 1982, *ApJ*, 263, 835
- Simonetti, J. H., Cordes, J. M., & Heeschen, D. S. 1985, *ApJ*, 296, 46
- Sousa, A. P., Alencar, S. H. P., Bouvier, J., et al. 2016, *A&A*, 586, A47
- Stauffer, J., Cody, A. M., Baglin, A., et al. 2014, *AJ*, 147, 83
- Stauffer, J., Cody, A. M., Rebull, L., et al. 2016, *AJ*, 151, 60
- Stelzer, B., Flaccomio, E., Briggs, K., et al. 2007, *A&A*, 468, 463
- Tofflemire, B. M., Mathieu, R. D., Ardila, D. R., et al. 2017, *ApJ*, 835, 8
- VanderPlas, J. T. 2018, *ApJS*, 236, 16
- Venuti, L., Bouvier, J., Irwin, J., et al. 2015, *A&A*, 581, A66
- Venuti, L., Cody, A. M., Rebull, L. M., et al. 2021, *The Astronomical Journal*, 162, 101
- Wang, X.-L., Fang, M., Herczeg, G. J., et al. 2023, *Research in Astronomy and Astrophysics*, 23, 075015
- Wenger, M., Ochsenbein, F., Egret, D., et al. 2000, *A&AS*, 143, 9
- White, R. J. & Basri, G. 2003, *ApJ*, 582, 1109
- Wright, E. L., Eisenhardt, P. R. M., Mainzer, A. K., et al. 2010, *AJ*, 140, 1868
- Zechmeister, M. & Kürster, M. 2009, *A&A*, 496, 577
- Zhao, G., Zhao, Y.-H., Chu, Y.-Q., Jing, Y.-P., & Deng, L.-C. 2012, *Research in Astronomy and Astrophysics*, 12, 723

## Appendix A: Details on light-curve filtering steps

### A.1. Bootstrap test for minimum light curve length

We performed bootstrap tests to determine the minimum number of epochs required to ensure statistically robust variability indices. As a baseline, we selected light curves of GAPS sources that contained the highest number of epochs (typically `num_selected_g_fov` between 70 and 100 observations). To account for variations of signal-to-noise as a function of observed magnitude, we selected 5 such sources within bins with 0.5 mag width for  $G$  between 6.5 and 20 mag. For each light curve selected, we computed the interquartile range (IQR) as a function of the total number of epochs while randomly removing epochs until only 10 epochs were left. To quantify the change introduced to the IQR by the removal of epochs, we computed a loss function as:

$$L_{IQR}(i) = \frac{|IQR_{original} - IQR(i)|}{IQR_{original}} \times 100, \quad (\text{A.1})$$

where  $IQR_{original}$  is the IQR of the original light curve and  $IQR(i)$  the IQR at the  $i^{th}$  step of epoch removal. The loss function represents a percentage difference between the original IQR and the IQR when points are removed.

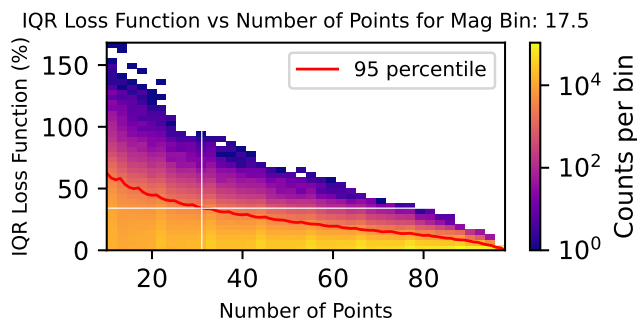


**Fig. A.1.** Heatmap of the IQR variations as a function of the number of epochs for sources in the magnitude bin around 17.5 mag based on a sample of 10 000 bootstrapped light curves. The red line shows the 95<sup>th</sup> percentile of the distribution. The white cross indicates the variation in the IQR for 95% of sources stays below 34.1% as long as the light curve includes at least 31 epochs.

We repeated the process 10 000 times per light curve to minimise biases introduced by specific epochs while randomly removing epochs. An example of the distribution of loss function values as a function of the number of epochs is shown in Fig. A.1 for the mag bin  $G = 17.5$ . Based on this distribution, we inferred the minimum number of epochs needed to keep the relative changes in the IQR under  $1\sigma$  (34.1%) of the original value for 95% of the light curves in that magnitude bin, which in the example shown in Fig. A.1 corresponded to 31 epochs. Fig. A.2 shows the minimum number of epochs as a function of magnitude for all magnitude bins considered. There is a strong peak between 9.5 and 13.5 mags, meaning sources with this magnitude have an IQR changing more intensely, which is likely related to Gaia’s instrumental effects around magnitude 12. To account for this feature, we applied a two-regime condition for the minimum number of observations and required at least 62 epochs for sources with magnitudes between 9.5 and 13.5 and 37 epochs for others.

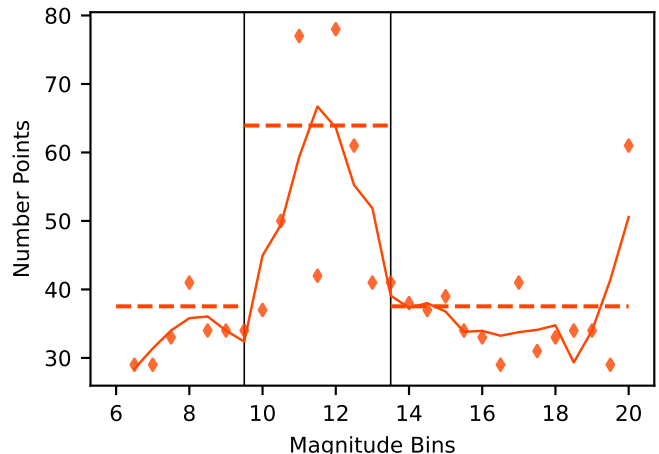


**Fig. A.2.** Minimum number of epochs needed to ensure the 95% of sources have an IQR variation under 34.1%, per mag bin. Diamonds show the raw values per mag bin. The solid line is a smoothed version. Vertical dotted lines show the 90 percentile of the points for a) mag bins between 9.5 and 13.5; b) other mag bins

### A.2. Spurious variability identification procedure

As part of GDR3, [Holl et al. \(2023\)](#) provides a series of parameters calculated to facilitate the identification of spurious variability signals introduced by Gaia’s complex scanning law and varying object scanning angles. These parameters were retrieved for our sources from the `vari_spurious_signals` table through [Gaia ESA Archive](#). In specific, we employed the pre-calculated Spearman correlation between photometric magnitudes and IPD GoF (Image Processing Data Goodness of Fit), `spearman_corr_ipd_g_fov`, and between magnitudes and their corrected flux excess factor `spearman_corr_exf_g_fov`. In both cases, a significant correlation suggests that scanning-law effects are likely present in the light curve.

Fig. A.3 shows the distribution of `spearman_corr_exf_g_fov` vs `spearman_corr_ipd_g_fov`, where the distribution is seen split into two bulks. We used a Gaussian Mixture model to isolate these two bulks, which allowed us to flag 22 375 sources in the YSO sample as likely affected by spurious variability. 187 sources had no `spearman_corr_exf_g_fov` and were also discarded.

#### A.2.1. Timescales in excess due to residual spurious variability

In Fig. A.4, we show a distribution of the power of the highest peak in the GLS periodogram as a function of the timescale for that peak (derived in Sect. 4.2.1). An excess of sources detected at specific long timescales (e.g., ~100, 50 and 25 d) is noticeable in this distribution. Fig. A.4 also shows a normalised frequency distribution of GLS timescales for sources affected by spurious variability identified in the previous section. Considering the timescales with at least 10% frequency among sources with spurious variability points to a correspondence of these with the timescales in excess, suggesting a prevalence of sources with spurious variability in our sample. We have further inspected these sources in the context of `spearman_corr_ipd_g_fov` and `spearman_corr_exf_g_fov` parameters discussed in the previous section to address if a different strategy could reduce their incidence. For example, the requirement that rather than

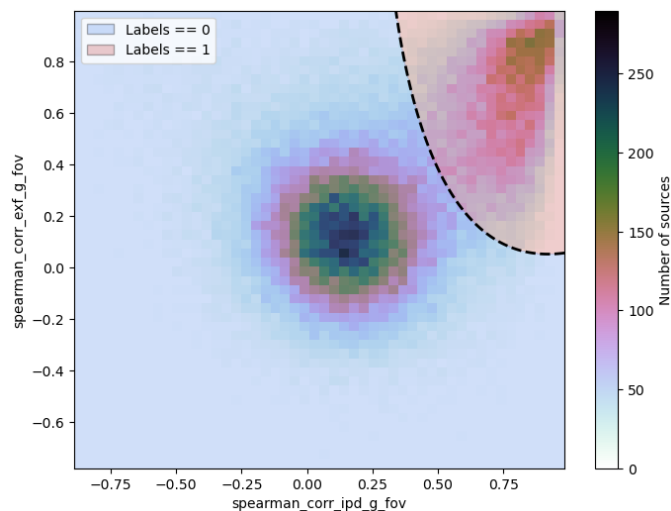


**Fig. A.3.** Distribution of Spearman correlations between Gaia’s field-of-view photometric magnitudes and their corrected flux excess factor (y-axis) and their Image Processing Data Goodness of Fit (x-axis) for 79 188 GDR3 YSOs. The distribution was split into separate Gaussian distributions, delimited by the blue and red shading.

both, either of these parameters show stronger correlation or using a lower correlation threshold. However, a relevant population of residual spurious variability sources was found even among sources with correlation values close to zero. In particular, we note that the recurrence of residual spurious variability is minimal within the primary (highly) variable sample defined in Sect. 3.5, but accentuated among sources in the secondary sample. Finally, we minimised this residual contamination by utilising the normalised frequency distribution of GLS timescales for sources affected by spurious variability identified in the previous section to mask the most frequent timescales among sources with spurious variability.

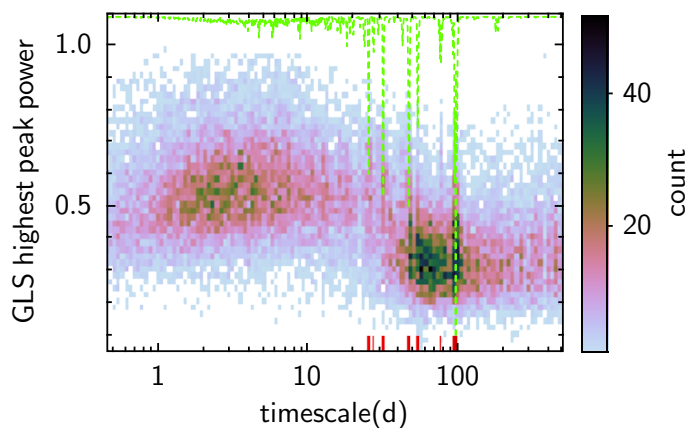


**Fig. A.4.** Density distribution of the power of the highest peak in the GLS periodograms as a function of their timescale for 34 739 variable sources analysed in Sect. 4.2.1, shown regardless of their FAL. The green dashed lines show the normalised frequency distribution of GLS timescales for sources affected by spurious variability introduced by Gaia’s complex scanning law and varying object scanning angles identified in Sect. A.2. This distribution is renormalised here for visualisation purposes. The red rugged lines highlight timescales in excess in our sample due to residual spurious variability, and masked from our sample.

### A.3. Procedure for outlier removal

Visual inspection of light curves exhibiting the highest peak-to-peak amplitude revealed that many of these sources had their variability and asymmetry analysis dominated by only one or two epochs beyond the  $5\sigma$  level. In the context of Gaia’s sparse light curves, we must address our capacity to judge whether these are spurious outliers or the results of the sparse sampling of a rapidly occurring variability event. For example, short-duration bursting features reported by Cody et al. (2017) typically span 10–20 days and typically show short duty cycles (time spent bursting). At certain latitudes, Gaia’s scanning law can occasionally yield the occurrence of a dozen observed epochs over a couple of days, a phenomenon often referred to as cusps (an example of Gaia DR3 light curve with a cusp is shown in Fig. 8 for the source *GDR3 3336474807652948992*). However, if not coincident with cusps, Gaia’s sparse sampling typically includes only one epoch every 10–20 days, henceforth under-resolving and, likely, often missing short-duration bursts.

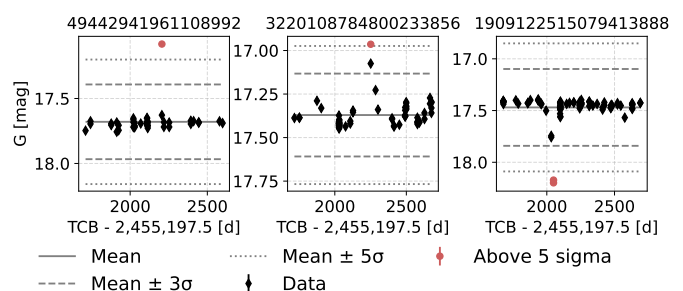
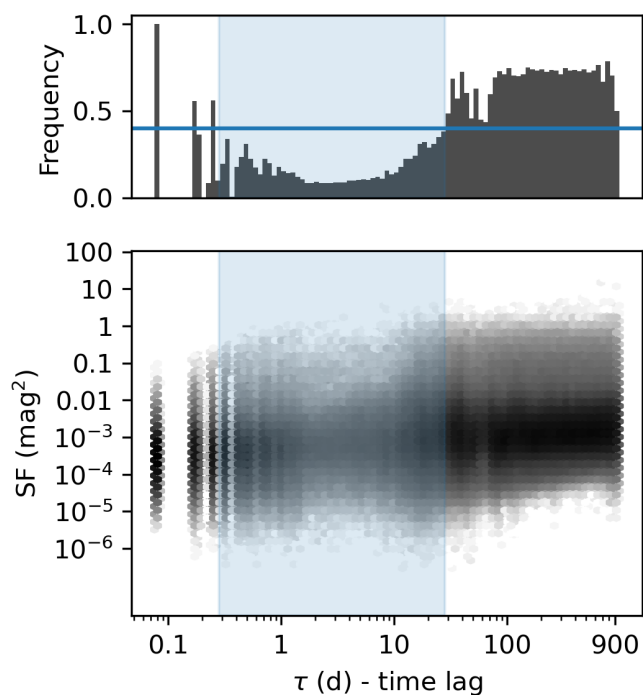


**Fig. A.5.** Examples of light curves with epochs beyond  $5\sigma$  level. *Left:* This epoch was not followed or preceded by a  $3\sigma$  outlier, and it was thus identified as an outlier and removed from the light curve. *Middle:* an example with a preceding epoch beyond the  $3\sigma$  level considered as a reliable variability feature. *Left:* Example with two successive epochs outside the  $5\sigma$  level also considered as a reliable variability feature.

We identified 735 sources (2% of the variable sample defined by Sect. 3.4) with at least one  $5\sigma$  outlier and only 11 having two outliers at the same level. We further hypothesise that finding these outliers at a systematically bursting behaviour could support the idea that these are undersampled but reliable rapid burst variables. However, we find an overall homogeneous distribution of outlier behaviour with about  $\sim 45\%$  flaring outliers versus  $\sim 55\%$  dimming outliers, thus denying our hypothesis. Including colour information could aid in further probing such events; nevertheless, colour variability was beyond the scope of the present study. We thus limit our approach to identifying and removing isolated outliers as follows. For each light curve with an epoch outside the  $5\sigma$  level, we evaluated if this epoch was isolated by examining if the immediately close epochs were at least within the  $3\sigma$  level while following the same bursting/dimming behaviour. If the epoch beyond the  $5\sigma$  level failed this criterion, it was considered an outlier and removed from the light curve. Fig. A.5 shows examples where the first light curve shows an example with an outlier, and two others show light curves with epochs outside the  $5\sigma$  level but identified as part of a reliable variability feature. 636 light curves had outliers removed with this criteria.

## Appendix B: Structure Function’s blind timescales

In this Appendix, we investigate the range of timescales affected by Gaia’s sparse time coverage. To this end, we employed



## Appendix C: Description of data table

Table C.1 provides an overview of the parameters used in this study, including source identifiers, astrometric and photometric properties, variability metrics, and classification results. The corresponding data table is available on Vizier.

**Fig. B.1.** *Bottom:* Structure function and time difference pairs considering all SF-points ( $\tau$ , SF) for all the 43 840 sources with enough number of epochs (Sect. 3.2). The blue region shows the depletion of pairs with  $\tau$  between 0.3 and 28 days, introduced by limitation in Gaia’s time-series sampling. *Top:* Distribution of  $\tau$  as a function of the frequency in which sources had a valid SF( $\tau$ ). The blue horizontal line shows the 40% limit used to infer Gaia’s blind timescale range.

Eq. 3 to calculate structure functions for all 43 840 sources with enough epochs in their light curves according to the procedure discussed in Sect. 3.2. Fig. B.1 shows the distribution of calculated  $\tau$ -SF( $\tau$ ) pairs at a population level, where a lower density of points is clearly seen at  $\tau$  values around  $\sim 1 - 10$  days. The frequency of  $\tau$ -SF( $\tau$ ) pairs occurrence is also shown in the top panel of Fig. B.1. We choose a conservative requirement of at least 40% to define a blind-SF range of timescales in the range  $\sim 0.3 - 28$  days. Nevertheless, we note that the issue of underpopulated SF is more critical for the timescale range of  $\sim 0.5 - 10$  days where any given  $\tau$ -SF( $\tau$ ) exists for less than 10% of sources. GDR3 scanning law (Fig. 1) implies that light curves will have varied sampling. Hence, the definition of this blind timescale range does not mean that timescales in this range cannot be measured with the SF method, but rather that SF will less frequently be well-sampled enough to detect such timescales. Based on the identification of this blind range, Sect. 3.2 includes additional processing steps to identify if an aperiodic timescale in this range came from an adequately sampled SF. Finally, we also note that this sampling issue is only expected to affect the SF method with the underlying assumption of an aperiodic SF model. For GLS periodic timescales, different underlying assumptions of a sinusoidal periodic signal apply, and various previous studies based on GDR3 light curves have corroborated its efficiency in detecting timescales in this range (e.g., Distefano et al. 2022).

**Table C.1.** Overview of the table contents used in this paper

Name	Description	Unit
source_id	GDR3 source identifier	
ra	Right ascension in ICRS at Gaia reference epoch	degree
dec	Declination in ICRS at Gaia reference epoch	degree
parallax	Absolute stellar parallax at Gaia reference epoch	mas
phot_g_mean_mag	G-band mean magnitude	mag
num_selected_g_fov	Number of G FOV transits selected for variability analysis by Gaia	
CTTS	If 0, no observational indication of ongoing accretion (WTTS). If > 0, at least one occurrence of ongoing accretion (CTTS). If null, no available information. See Sect. 5.3.1.	
alpha_ir	$\alpha_{\text{IR}}$ index. See Sect. 5.3.2.	
timescale_method	GLS if the GLS periodogram was used to get the timescale (Sect. 4.2.1). SF if the structure function was used (Sect. 4.2.2).	
timescale	Dominant timescale, if not larger than half the light-curve duration	days
long_timescale_method	GLS if the GLS periodogram was used to get the timescale. SF if the structure function was used. Null if the dominant timescale is not long.	
long_timescale	Dominant timescale, if larger than half the light-curve duration	days
primary	True if the source is part of the primary sample. False if the source is part of the secondary sample. See Sect. 3.5.	
Q_index	Q-index value from Eq. 1	
M_index	M-index value from Eq. 2	
amplitude	Peak-to-peak amplitude of the G-band light curve	mag
morphological_class	Morphological class inferred from Q&M indices. Can be P, EB, QPS, QPD, B, S, APD, L (Sect. 4.4).	